

## High-resolution experimental and theoretical study of singly and doubly excited resonances in ground-state photoionization of neon

Konrad Schulz, Michael Domke, Ralph Püttner, Alejandro Gutiérrez, and Günter Kaindl  
*Institut für Experimentalphysik, Freie Universität Berlin, Arnimallee 14, D-14195 Berlin-Dahlem, Germany*

Gregory Miecznik and Chris H. Greene  
*Department of Physics and Joint Institute for Laboratory Astrophysics, University of Colorado, Boulder, Colorado 80309-0440*

(Received 8 February 1996)

An experimental and theoretical study of ground-state photoionization of neon is presented in the photon energy range between 44 and 53 eV. This portion of the spectrum is characterized by a singly excited Rydberg series  $2s2p^6np$ , and by overlapping doubly excited Rydberg series  $2s^22p^43snp$  and  $2s^22p^43pnl$  ( $l=s,d$ ). With the use of synchrotron radiation of  $\approx 3$  meV spectral resolution, numerous hitherto unobserved resonances were resolved, including some which exhibit relativistic effects. To identify resonances observed here and in earlier works, we employed numerical calculations, which combine the eigenchannel  $R$ -matrix method, multichannel quantum defect theory, and the recoupling frame transformation. These nearly *ab initio* methods account for most of the observed features in the spectrum, including a class of spin-induced relativistic effects. [S1050-2947(96)10410-8]

PACS number(s): 32.80.Fb, 31.50.+w

### I. INTRODUCTION

Photoionization of the ground state of neon is characterized, at photon energies from 44 to 53 eV, by a singly excited  $2s2p^6np$  autoionizing Rydberg series and by overlapping doubly excited  $2p^43snp$  and  $2p^43pnl$  ( $l=s,d$ ) autoionizing Rydberg series. The doubly excited resonances can be photoexcited mainly through the presence of electron correlations in the initial state  $2s^22p^6^1S$ . Thus these series typically appear with very low intensities in the photoionization cross section. The decay dynamics of these Rydberg states is complicated by strong interchannel interactions and by the numerous competing autoionization paths — all states decay into the singly excited  $2p^5\epsilon l$  continua and, if allowed by energy conservation, into other doubly excited continuum channels  $2p^43s\epsilon p$  and  $2p^43p\epsilon l$  ( $l=s,d$ ) [1].

In a pioneering work of neon excitation, Codling *et al.* [2] measured the absorption spectrum at photon energies from 44 to 64 eV. However, owing to their limited 12 meV resolution, all of the spectral features reported here were not resolved. Higher-resolution photoionization experiments in the VUV energy range have recently been conducted for rare-gas atoms [1,3–9]; a comprehensive review of many experimental aspects can be found in Ref. [10]. Of particular relevance to our work are Refs. [3,4], which report preliminary results on single and double excitations in neon photoionization cross section, using the high-resolution SX700/II monochromator. In the present paper we report on improved measurements for the neon photoionization; apart from refining the spectrum measured by Codling *et al.* [2], our experiment, whose spectral resolution is about 3 meV in the photon energy range between 44 and 53 eV, unveils the previously unresolved resonances  $2p^4(^3P)3s(^2P)4p$  and  $2p^4(^3P)3s(^2P)5p$ , and brings up relativistic features of highly excited resonances converging to different fine-structure thresholds associated with the  $2p^4(^3P)3s^2P$  and  $2p^4(^3P)3p^2P$  states of  $\text{Ne}^+$ .

Theoretical studies of rare-gas atom photoionization are well established below the second fine-structure split threshold  $np^5^2P_{1/2}$  [10,11]. However, studies above this threshold (i.e., above the first ionization threshold in  $LS$  coupling), which specifically include a resonance structure, still pose nontrivial difficulties. In much earlier studies, Burke and Taylor [12] investigated the singly excited resonances  $nsnp^6n'p$  in neon ( $n=2$ ) and in argon ( $n=3$ ); the  $nsnp^6n'p$  resonances were studied also very recently in neon [13] and in neon through krypton [14]. The total and partial cross sections in the direct photoionization of outer shells in neon through xenon were investigated over a broad energy range [15], although the resonance structure was ignored in these studies. While double excitations in argon were studied recently [16], no line-by-line comparison with the experiment was reported. Reference [10] reviews some recent computational studies in the rare-gas atoms, including helium.

Calculations of the resonance structure in rare-gas atoms are hampered due to the high excitation energies of the target states, due to the large number of strongly interacting channels, and due to the importance of correlation effects. These and other difficulties also plague the present eigenchannel  $R$ -matrix studies, where we treat doubly excited resonances in a system with many valence electrons, and over a wide energy range. Earlier eigenchannel  $R$ -matrix calculations applied to open  $p$ -shell atoms [17,18] and to transition-metal atoms [19,20] treated only single-electron excitations over a range of energies limited to just a few eV above the first ionization threshold. Those earlier studies successfully explained many features in those strongly perturbed spectra. The present calculations show that the same methods also provide spectroscopically useful information and a comprehensive picture of the neon photoionization over an energy range approximately 10 eV in breadth.

## II. EXCITATION MECHANISM IN NEON

### A. Overview of doubly excited Rydberg states

A photon in the energy range between 44 and 53 eV can excite a Ne  $2s$  electron,  $2s^2 2p^6 \rightarrow 2s 2p^6 np$ , or it can excite two  $2p$  electrons (via correlation effects discussed in Sec. II B) into one of several Rydberg series,  $2p^6 \rightarrow 2p^4 n l n' l'$  [1,2]. Here,  $nl$  is  $3s$  or  $3p$ , and  $n' l'$  labels an excited  $s$ ,  $p$ ,  $d$ , or  $f$  electron which couples to an odd-parity state of Ne. For brevity, we omit the filled  $2s$  core from our notation for the doubly excited states. A variety of doubly excited Rydberg series arise from the allowed configuration of  $2p^{-2}$  Ne atom:  $2p^4(^3P)$ ,  $2p^4(^1D)$ , and  $2p^4(^1S)$ . Since the majority of the Rydberg series observed in this portion of the neon spectrum can adequately be described within a nonrelativistic  $LS$  approximation, we treat here only  $^1P^o$  final states. Relativistic effects are discussed in Sec. II C.

The following  $^1P^o$  double excitation Rydberg series can be formed: three  $3snp$  series:

$$2p^4 \begin{pmatrix} ^3P \\ ^1D \\ ^1S \end{pmatrix} 3s \begin{pmatrix} ^2P \\ ^2D \\ ^2S \end{pmatrix} np \ ^1P^o,$$

three  $3pns$  series:

$$2p^4 \begin{pmatrix} ^3P \\ ^1D \\ ^1S \end{pmatrix} 3p \begin{pmatrix} ^2P \\ ^2P \\ ^2P \end{pmatrix} ns \ ^1P^o,$$

and six  $3pnd$  series:

$$2p^4 \begin{pmatrix} ^3P \\ ^1D \\ ^1S \end{pmatrix} 3p \begin{pmatrix} ^2D, ^2P \\ ^2F, ^2D, ^2P \\ ^2P \end{pmatrix} nd \ ^1P^o.$$

Higher excitations  $3dnp$ ,  $3snf$ ,  $4fns$ ,  $3dnf$ , etc., do not appear in the neon spectrum below 53 eV, except for the lowest perturbers (see below). In  $LS$  coupling, if fine-structure effects are neglected, only the  $2s$  singly excited and five double excited Rydberg series need to be considered below 53 eV. These are  $2s 2p^6(^2S)np$ ,  $2p^4(^3P)3s(^2P)np$ ,  $2p^4(^1D)3s(^2D)np$ ,  $2p^4(^3P)3p(^2D)nd$ , and  $2p^4(^3P)3p(^2P)nd$ ; each of these is coupled to the final symmetry  $^1P^o$ . An  $nf$  series converging to  $2p^4(^1D)3s^2D$  can also be excited, but only the lowest member  $4f$  has been resolved. Additionally, the  $2p^4(^1S)3s(^2S)3p$  member of a higher series is energetically allowed. Among members associated with other Rydberg series, also the  $2p^4(^3P)3d(^2D)3p \ ^1P^o$  and  $2p^4(^3P)3d(^2P)3p \ ^1P^o$  resonances can be photoexcited in this photon energy range. Note, however, that each of these states can be formed from a linear combination of  $2p^4(^3P)3p(^2D)3d \ ^1P^o$  and  $2p^4(^3P)3p(^2P)3d \ ^1P^o$  wave functions. Consequently,  $2p^4(^3P)3d(^2D)3p \ ^1P^o$  and  $2p^4(^3P)3d(^2P)3p \ ^1P^o$  represent the same physical states as given by  $2p^4(^3P)3p(^2D)3d \ ^1P^o$  and  $2p^4(^3P)3p(^2P)3d \ ^1P^o$ . Similarly,  $2p^4(^1D)3p(^2P)3s \ ^1P^o$  is the same physical state as  $2p^4(^1D)3s(^2D)3p \ ^1P^o$ . In Fig. 1, an energy level diagram of neon is given, and energies of

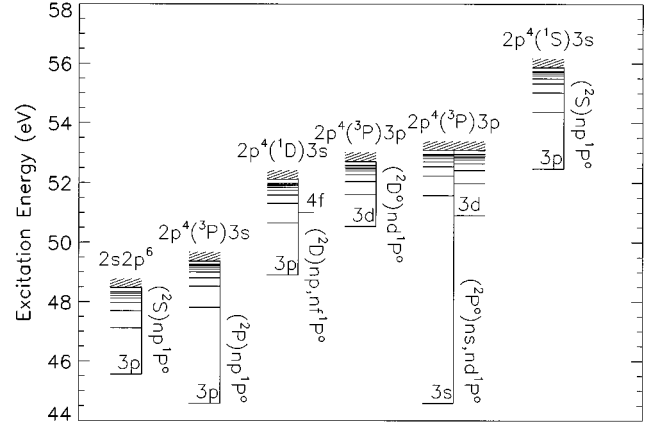


TABLE II. A shorthand wave function expansion of the initial ground state  $2s^22p^61S$ . Only those components, whose weight  $|c_k|^2$  is larger than 0.001, are tabulated. The  $2s$ ,  $2p$ ,  $3s$ , and  $3p$  are spectroscopic orbitals describing the target states,  $\bar{4}s$ ,  $\bar{4}p$ , and  $\bar{3}d$  are correlation orbitals also used in the target-state representation.

Component	Weight
$2s^22p^6$	0.89886
$2s^22p^5(^2P)3p$	0.05583
$2s^22p^5(^2P)\bar{4}p$	0.01519
$2s2p^6(^2S)3s$	0.00380
$2s2p^6(^2S)4s$	0.00206
$2s^22p^4(^3P)\bar{3}d^2$	0.00324
$2s^22p^4(^1D)\bar{3}d^2$	0.00195
$2s^22p^4(^1S)\bar{3}d^2$	0.00159
$2s^22p^4(^1D)3p^2$	0.00205
$2s^22p^4(^3P)3p^2$	0.00136

detail in the present paper. In Sec. V we analyze in addition the  $4p$  and  $5p$  members of the  $2p^4(^3P)3s(^2P)np$  series interacting with the singly excited  $2s2p^6np$  series, a quenching of the  $2p^4(^1D)3s(^2D)np$  resonances ( $n>9$ ) by the  $2p^4(^3P)3p(^2P)5s$  perturber, and an interference between  $2p^4(^1S)3s(^2S)3p$  and highly excited  $ns$  and  $nd$  series converging to the  $2p^4(^3P)3p^2P$  ionization threshold.

### B. Excitation paths from the ground state to the doubly excited states

Photoexcitations from the ground state to the doubly excited states are possible mainly to the extent that the initial state exhibits electron correlation. Dipole transitions induced in this way favor only some final states, thus different Rydberg series listed above will have very different spectral intensities. Table II shows a shorthand configuration interaction (CI) expansion of the initial ground state  $2p^61S$ , whose calculations are outlined in Sec. IV B. The  $2p^6$  configuration contributes 90% to the wave function expansion (i.e., the square of its CI coefficient is 0.9), whereas the next largest configuration  $2p^53p$  contributes nearly 6%.  $2p^53p$  represents, in the independent particle model, radial correction, i.e., a difference in the spatial distribution between Ne and  $\text{Ne}^+$  ground-state configurations, if one assumes that the radial orbitals are optimized independently on each configuration. Other  $2p^5np$  configurations ( $n>3$ ) also represent the radial correction, but to much lesser extent.

The radial correction allows for dipole-induced transitions to all of the observed  $2p^43l3l'$  members, where  $l$  and  $l'$  are  $s$ ,  $p$ , or  $d$  electrons. Dipole transitions to excited members of the Rydberg series  $2p^43snp$  ( $n>3$ ) are excluded because  $np$  orbitals representing the final states are orthogonal to the  $3p$  orbital in the  $2p^53p$  initial state configuration. These series can be reached only through the admixture of other initial state configurations, such as  $2p^5np$ , which, however, contribute less than 0.15% to the wave function expansion. Therefore, all  $3snp$  series will have, in general, very weak spectral intensities. An exception is the  $2p^4(^3P)3s(^2P)np$  Rydberg series, which is greatly enhanced owing to an inter-

action with a  $2p^4(^1D)3s(^2D)3p^1P$  perturber (see Sec. V B).

Among excited  $2p^43pns$  and  $2p^43pnd$  members ( $n>3$ ), all of the  $3pns$  series and some of the  $3pnd$  Rydberg series can be photoexcited through the radial correction. Electric dipole selection rules permit the following transitions to occur

$$2p^5(^2P)3p^1S \xrightarrow{2p \rightarrow nl} \begin{cases} 2p^4(^3P)3p(^2P)nl^1P^o \\ 2p^4(^1D)3p(^2P)nl^1P^o \\ 2p^4(^1S)3p(^2P)nl^1P^o \end{cases} \quad (1)$$

where  $l=s,d$ . Thus all  $3pns$  series will be strong in the spectrum and will have the highest photoabsorption strength among all doubly excited resonances. However, among these series, only  $2p^4(^3P)3p(^2P)nl^1P^o$  are energetically accessible for photon energies below 53 eV.

Those  $3pnd$  Rydberg series which are not listed above, as  $2p^4(^3P)3p(^2D)nd^1P^o$ , are much weaker since they can be photoexcited only through the admixture of other, less important, initial state configurations. Actually, only the lowest member  $2p^4(^3P)3p(^2D)3d^1P^o$  was observed in the earlier photoabsorption spectrum [2] and in the present high-resolution experiment. Higher excited members have not been resolved and they appear to be very weak in the calculated spectrum.

Codling *et al.* [2] noted that the lowest Rydberg series members  $n=3$  are much more intense than excited members with  $n>3$ . A prominent example is the lowest resonance  $2p^4(^3P)3s(^2P)3p^1P^o$  in the neon spectrum, which is far stronger than the  $3s4p$  and  $3s5p$  resonances. In fact, these two latter Rydberg series members were not resolved in the early spectrum [2]. This observation contradicts a general trend, that all members in an unperturbed Rydberg series, with no Cooper minimum, have the same maximum photoabsorption cross section (provided the spectrum is measured with an infinite resolution). As pointed out, the  $3s3p$  members are photoexcited with a much higher probability than  $3snp$  members with  $n>3$ . Moreover, the  $n=3$  resonances are confined almost entirely within the inner core (which extends to about 12 Bohr radii) and thus experience stronger electron correlations than the higher- $n$  members [1]. This, in turn, causes a departure in the quantum defect and can enhance the photoabsorption strength.

### C. Breakdown of $LS$ coupling

If we ignore the fine-structure splitting of  $\text{Ne}^+$  states, which, on the average, are of the order of 10 meV,  $LS$  coupling is satisfied for most of the resolved resonances in the spectrum. However, even in the comparatively low-resolution experiment by Codling *et al.* [2], one could resolve fine-structure splitting of the  $2p^4(^3P)3s(^2P)np$  series ( $n\geq 6$ ) into  $3s(^2P_{3/2})np$  and  $3s(^2P_{1/2})np$  series. Table I shows that  $2p^4(^3P)3s^2P$  has the largest fine-structure splitting among all relevant doublet states of  $\text{Ne}^+$ ,  $\Delta E_{j_c} = 75.9$  meV. In our high-resolution experiments, the splitting into three series that converge to two  $j_c$ -dependent thresholds is observed already for the  $n=4$  members. Similar features are also observed for the  $ns$  and  $nd$  Rydberg series converging

to  $2p^4(^3P)3p^2P_{j_c}$ . However, due to the smaller target state splitting  $\Delta E_{j_c} = 15.8$  meV, the fine-structure effects in the  $2p^4(^3P)3p(^2P_{j_c})nl$  series are resolved for higher members ( $n \geq 7$ ) than in the  $2p^4(^3P)3s(^2P_{j_c})np$  series ( $n \geq 4$ ). In Sec. IV A we discuss briefly how the size of the target fine-structure splitting affects the intensity of the fine-structure split Rydberg series.

The fine-structure split Rydberg series are described best in  $jj$  coupling  $(j_c, j_o)_n$ , where  $j_c$  and  $j_o$  are the total momentum of the target state and of the outermost electron, respectively, [for example, the  $2p^4(^3P)3s(^2P_{j_c})np$  series], or in  $jK$  coupling  $[(j_c, l_o)K, s_o = 1/2]J=1$ , abbreviated  $[(j_c, l_o)K]$  [for example, the  $2p^4(^3P)3p(^2P_{j_c})nl$  ( $l = s, d$ ) series]. These and other relativistically coupled series can be recoupled to  $LS$  representation of  $^1P_1^o, ^3S_1^o, ^3P_1^o, ^3D_1^o$  states. Only these  $LS$  symmetries are relevant here, since dipole transitions occur between levels which differ by  $\Delta J = 0, \pm 1$ , excluding  $J=0 \rightarrow J=0$  transitions, and symmetries with higher  $L$  and  $S$  quantum numbers, for example,  $^5F_1^o$ , can be formed only by coupling an outer electron with a  $\text{Ne}^+$  quartet state; however, as we mentioned earlier, such states are not expected to contribute significantly to the total cross section.

### III. EXPERIMENTAL TECHNIQUES

Neon atoms are excited by a single photon from a highly monochromatized photon beam at the Berliner Elektroenspeicherring für Synchrotronstrahlung (BESSY) [3]. Photoexcitation is measured by collecting the charged particles which are produced via the decay of the excited neon by direct photoionization or by autoionization. The total photoionization current in the  $10^{-12}$  A range is measured as a function of photon energy. These photoionization measurements were performed with a two-plate ionization cell of 10 cm active length [3], filled with neon gas, whose pressure was between 0.1 and 1 mbar; the cell was separated from the ultrahigh vacuum of the monochromator by a 1500 Å Al(1% Si) window. A voltage of 100 V was applied between the two plates to collect the electrons and ions, and the current was measured with a sensitive ammeter (Keithley, model 617). The measured current is proportional to the photoabsorption cross section only in case of low gas density, i.e., for a linear approximation to the Lambert-Beer law. Note that in the case of weak resonances quite large neon pressures are needed, and minor saturation effects influencing the accurate line shape and the natural linewidth of a resonance cannot be excluded [7]. Note in addition, that these measurements can give only *relative* cross sections rather than absolute cross sections, because it is difficult to correct for a background caused by the production of photoelectrons from the Al window and by an approximately linear beam decay as well as the energy-dependent monochromator intensity function.

For the high-resolution photoexcitation measurements, a very narrow energy width  $\Delta E$  was obtained from the high-resolution SX700/II monochromator operated by the Freie Universität Berlin at BESSY [3]. This monochromator is equipped with a plane premirror, a plane grating (2442 lines/mm), and an ellipsoidal mirror focusing the fixed (virtual)

beam source onto a curved exit slit (3  $\mu\text{m}$ ). The monochromator has no entrance slit, and thus position and size of the electron beam source influence strongly both energy calibration and resolution. Nearly all measurements were performed with BESSY operating in the small-source mode (vertical beam size  $\cong 0.12$  mm) and a 20% illuminated portion of the ellipsoidal mirror. Usually, the photon energy is adjusted by moving *both* the plane mirror and the grating in order to get fixed foci of the ellipsoidal mirror; then, the resolution  $\Delta E$  scales with  $E^{3/2}$ . However, the incidence angle of the premirror is restricted to a value lower than  $13^\circ$  [21], and the monochromator no longer works in the so-called “fix-focus mode” for low photon energies ( $h\nu < 76$  eV for the 2442 lines/mm grating), i.e., the energy range relevant at present. Instead, photon energies are adjusted by rotating only the grating with the premirror fixed: here resolution is optimized by changing the distance between the ellipsoidal mirror and the exit slit adjusting the exit slit to the varying focus. As a consequence, of course, the usual scaling of the resolution  $\Delta E$  with  $E^{3/2}$  does not apply, and we need an independent check of the resolution: we get a resolution of  $\Delta E \cong 4$  meV (FWHM) [6] at  $h\nu = 64$  eV and of  $\Delta E \cong 3$  meV (FWHM) at  $h\nu = 45\text{--}53$  eV by shifting the exit slit by 9 mm and 20 mm, respectively. Also the photon energy cannot be calibrated using “fix-focus mode” energy values, obtained, e.g., for the well known helium double excitations [6]. Here the photon energy was calibrated by fitting the  $2s2p^6np$  resonances with a Rydberg series of Fano profiles with a constant quantum defect, presuming the  $2s2p^6$  threshold to be at 48.4750 eV. This threshold is taken from the well-known literature value of the Ne II  $2s2p^5$  level at  $217\,047.61\text{ cm}^{-1}$  (26.9105 eV) [22], added to the lowest neon ionization threshold,  $2s^22p^5^2P_{3/2}$ , at  $173\,929.70\text{ cm}^{-1}$  (21.5645 eV) [23], using the conversion:  $1\text{ cm}^{-1} = 0.123\,984\,2\text{ meV}$  [24].

### IV. THEORETICAL AND COMPUTATIONAL METHODS

#### A. Principles

The theoretical and computational methods adopted in this study are the same as in the earlier eigenchannel  $R$ -matrix studies [18–20]. We use the eigenchannel  $R$ -matrix method [17], multichannel quantum defect theory (MQDT) [25], and the recoupling frame transformation [26]. In this section we mainly describe the construction of the basis functions needed to calculate the initial and final state wave functions inside the region where strong interactions are localized, the so-called “reaction zone.”

Any wave function for the  $(N+1)e^-$  system ( $\text{Ne}^+, e^-$ ) is characterized by a coupling between a target state ( $\text{Ne}^+$  state) and an outermost electron. The eigenchannel  $R$ -matrix method solves, utilizing a variational principle, the  $(N+1)$ -electron dynamics inside a region of strong correlation. This region is characterized by an  $R$ -matrix sphere of radius  $r = r_0$ , which is large enough to envelope all relevant  $\text{Ne}^+$  states and the ground state of Ne. It is also large enough so that one can neglect electron-induced multiple potentials (which appear in close-coupling equations) between the outermost electron and the residual ion. In our calculations we chose  $r_0 = 12$  Bohr radii. The target state wave functions, whose decay are sufficiently rapid that they can be neglected

at  $r > r_0$ , are constructed in a multiconfiguration Hartree-Fock approximation [27], whereas the outermost electron wave function is represented inside the  $R$ -matrix sphere by a superposition of discretized orbitals, which obey a Hartree equation inside  $r < r_0$ . After the  $R$ -matrix calculation determines the  $(N+1)e^-$  wave function and its normal derivative at the surface  $r=r_0$ , MQDT determines the wave function everywhere outside  $r_0$ . This outer MQDT solution can be characterized by a reaction matrix at all distances  $r > r_0$ :

$$\Psi_i(r) = A \frac{1}{r} \sum_j \Phi_j(\omega) [f_j(r) \delta_{ji} - g_j(r) K_{ji}]. \quad (2)$$

Elements of the short-range MQDT reaction matrix  $\underline{K}$  are determined by matching the inner and outer solutions and their radial derivatives at  $r=r_0$ . Here,  $f$  and  $g$  are two standard, linearly independent Coulomb functions. In an energy range where autoionization can occur, i.e., where some ionization channels are energetically ‘‘open’’ (channels labeled  $o$ ) and other channels are ‘‘closed’’ (labeled  $c$ ), we must superpose the linearly independent solutions in Eq. (2) so as to eliminate diverging solutions in the closed channels. This resulting linear transformation of the solutions (2) generates a *physical* reaction matrix  $\underline{K}^{\text{phys}}$ ,

$$\underline{K}^{\text{phys}} = \underline{K}^{oo} - \underline{K}^{oc} (\underline{K}^{cc} + \tan \pi \underline{\nu})^{-1} \underline{K}^{co}, \quad (3)$$

where the diagonal matrix of effective quantum numbers in the closed channels is given by

$$\underline{\nu}_{ij} = \frac{1}{\sqrt{2(E_j - E)}} \delta_{ij}. \quad (4)$$

The matrix  $\underline{K}^{\text{phys}}$  connects only open channels to each other. A similar transformation is also applied to dipole matrix elements  $\underline{D}$  connecting the initial and final states. We use experimental target state energies  $E_j$  to evaluate the elements of  $\underline{\nu}$ , whereas theoretical energies are used to determine the short-range parameters  $\underline{K}$  and  $\underline{D}$ . The short-range parameters  $\underline{K}$  and  $\underline{D}$ , along with the threshold energies, uniquely determine the total and partial photoionization cross sections [25].

As pointed out in Sec. II C, some portions of the neon spectrum exhibit relativistic effects. In particular, three  $np$  series are found to converge to different fine-structure levels  $j_c = \frac{3}{2}$  and  $j_c = \frac{1}{2}$  of the residual  $\text{Ne}^+$  ion  $2p^4(^3P)3s^2P$ . The relativistic effects are incorporated by transforming the wave functions, and consequently  $\underline{K}$  and  $\underline{D}$ , from  $LS$  coupling into  $jj$  coupling (or into any equivalent coupling scheme for which the total core spin-angular momentum  $j_c$  is a good quantum number) [26]. In addition to performing this orthogonal transformation, it is crucial to use experimental fine-structure target state energies when the effective quantum numbers are evaluated in Eq. (3).

The fine-structure effects are the strongest for those Rydberg series whose ionization thresholds have the largest splittings  $\Delta E_{j_c}$ . Then, even low-lying members exhibit a  $j_c$ -dependent splitting. This can be understood from semiclassical arguments derived from the WKB approximation [28], which relate the size of the target state splitting to a cumulative phase change in the de Broglie wave of the outer

electron  $\Delta\varphi \cong \int dr \sqrt{2E_{j_{c_1}} + 2/r} - \int dr \sqrt{2E_{j_{c_2}} + 2/r}$  [29]. In the limit  $E \rightarrow 0$ , i.e., close to the ionization threshold, the phase change  $\Delta\varphi$  between channels associated with different fine-structure levels depends on the electronic distance  $r$  as  $(\sqrt{2}/3)r^{3/2}\Delta E_{j_c}$ . Thus for each fine-structure split Rydberg series, there is a limiting value of  $r$  which approximately marks a transition from a nonrelativistic  $LS$  coupling to a relativistic  $jj$ , or  $jK$  coupling. Its value, which directly translates into an effective quantum number of a Rydberg state, depends on the size of the target state splitting  $\Delta E_{j_c}$  and on the difference between quantum defects in the relevant  $LS$ -coupled Rydberg series. For these reasons, low-lying Rydberg series members tend to be nearly pure  $LS$ -coupled states, and thus spin-forbidden excitations to low- $n$  resonances are very weak. In contrast, highly excited Rydberg states are better characterized in either  $jj$  or  $jK$  coupling, and excitations to all fine-structure split components of a given  $n$  state can be comparably important.

## B. Calculations of the relevant $\text{Ne}^+$ target states

The first step in the calculations is the generation of atomic wave functions for the physically relevant target states, which contribute to the initial state  $2s^22p^6^1S$ , to the ionization continua, and to the resonances of  $^1P^o$  symmetry below 53 eV (see Sec. II A). The following  $\text{Ne}^+$  doublet states are needed:  $2p^5^2P^o$ ,  $2s2p^6^2S$ ,  $2p^4(^3P)3s^2P$ ,  $2p^4(^1D)3s^2D$ ,  $2p^4(^3P)3p^2D^o$ ,  $2p^4(^3P)3p^2P^o$ , and  $2p^4(^1S)3s^2S$ . We have tested the inclusion of  $\text{Ne}^+$  quartet states associated with the doubly excited  $2p^43s$  and  $2p^43p$  configurations, and found their contribution to be negligible. Furthermore, in all cases but one (see Sec. V A), resonances associated with those quartet states have not been observed.

Target orbitals are calculated in a multichannel Hartree-Fock approximation (MCHF) [27,30], where we include both spectroscopic and correlation orbitals. In what follows we overline correlation orbitals, for example  $\overline{4p}$ , to distinguish them from spectroscopic orbitals of the same angular symmetry, such as  $2p$  or  $3p$ . First, the  $1s$ ,  $2s$ , and  $2p$  orbitals are optimized on the  $2p^5$  configuration, then  $3p$  is optimized on  $2p^43p$  (averaged over  $LS$  term values), and  $3s$  on  $2p^43s$ . Next, we optimize correlation orbitals  $\overline{n\ell}$  on those physical  $\text{Ne}^+$  states, which are strongest correlated.  $\overline{4s}$  is optimized on  $2p^4(^3P)3p^2P^o$ , including single- and double-electron substitutions from the  $2s$ ,  $\overline{2p}$ , and  $3p$  subshells to a virtual  $\overline{4s}$  orbital, similarly  $\overline{4p}$  is optimized on  $2p^4(^1D)3p^2D^o$ , including single- and double-electron substitutions, and  $\overline{3d}$  is optimized on  $2s2p^6^2S$ , including a  $2p^4\overline{3d}^2S$  perturber.

The correlation orbitals play an essential role in the description of all physical  $\text{Ne}^+$  states. The largest correlation is observed for  $2s2p^6^2S$ , where the  $2p^4\overline{3d}^2S$  perturber contributes nearly 25% to the wave function expansion. This strong correlation in rare-gas atoms was recognized in earlier studies by other authors [13,16,31]. There is a large difference, however, in the nature of the  $3d$  orbitals in neon and in the heavier rare-gas atoms. In argon, a spectroscopic  $3d$  orbital is contracted within the same space (about 15 a.u.) as the  $3s$  and  $3p$  orbitals, and it strongly correlates with the

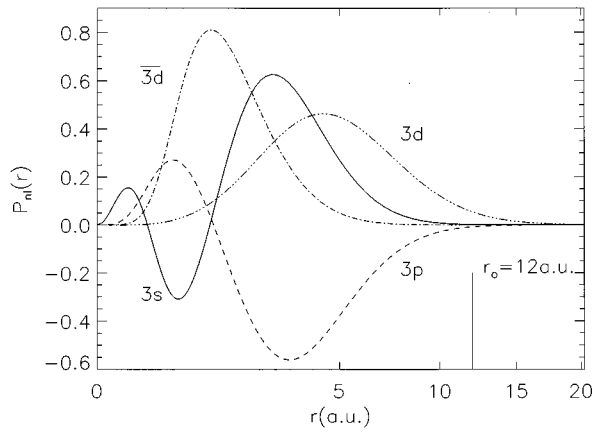


FIG. 2. Spectroscopic  $3s$  and  $3p$ , and a correlation  $\bar{3}d$  radial orbital  $P_{nl}(r)$  used in the calculation of  $2p^5$ ,  $2s2p^6$ ,  $2p^43s$ , and  $2p^43p$  target states of  $\text{Ne}^+$ . The  $\bar{3}d$  orbital strongly correlates  $2s2p^62S$  through interaction with  $2s^22p^4(^1D)\bar{3}d^2S$ . All these target states fit within 12 Bohr radii. For comparison we also plot a spectroscopic  $3d$  orbital which represents  $2p^4(^3P)3d$  target states of  $\text{Ne}^+$ . The  $2p^4(^3P)3d$  states extends up to 20 Bohr radii. The scale on the horizontal  $x$  axis is evenly distributed in  $\sqrt{r}$ .

$3s3p^6$  configuration. In contrast, the spectroscopic orbital  $3d$  in neon extends up to at least 20 a.u., and has little effect on the  $2s2p^6$  configuration which is confined within  $\cong 6$  a.u. Therefore, to correlate  $2s2p^6$  one has to use a correlation orbital  $\bar{3}d$ , which can be concentrated in the same region of space as the  $2s$  and  $2p$  orbitals. Other correlation orbitals in neon, as  $\bar{4}p$  in the CI expansions for  $2p^43p$ , are needed to represent both the proper correlation (pair correlation  $2p^2 \rightarrow \bar{4}p^2$ ), and to represent a radial correction ( $2p \rightarrow \bar{4}p$  and  $3p \rightarrow \bar{4}p$ ). For example, the radial correction is necessary because spectroscopic  $2p$  and  $3p$  orbitals are different for the different configurations. Figure 2 illustrates spectroscopic  $3s$ ,  $3p$ ,  $3d$ , and a correlation  $\bar{3}d$  orbital in  $\text{Ne}^+$ .

The MCHF orbitals are now used to construct the physical target states. In the first step we generate a long CI expansion for each state, including singly and doubly excited configurations from each occupied subshell in the  $2p^5$ ,  $2s2p^6$ ,  $2p^43d$ , or  $2p^43p$  configurations to  $2s$ ,  $2p$ ,  $3s$ ,  $3p$ ,  $\bar{3}d$ ,  $\bar{4}s$ , and  $\bar{4}p$  orbitals, following the parity conservation and the spin- and angular-momentum coupling rules. To the above CI expansion, we also add some configurations representing the core polarization, as constructed from single-electron excitations from the main configuration for each physical target state, involving the parity change. In particular, they are represented by  $2p^43s$ ,  $2p^43p$ , and  $2p^43d$ , with all allowed final couplings. A nonrelativistic Hamiltonian is diagonalized in this large basis, thereupon it is truncated to include only those components for each physical target state, whose weight is larger than 0.0005. On the average, we keep about 15 configurations for each physical target state.

Table I shows our theoretical target state energies relative to the ground state  $2p^61S$  in comparison with experimental values from Persson [22]. The energies of the first threshold  $2p^52P^o$  are assumed equal in this comparison. The largest error of our theoretical values of the excitation energy is about 0.4 eV, which translates into an error of order of 0.02

in a quantum defect calculated with respect to the double-ionization threshold  $2p^43P_2$  at 62.527 eV; from other eigenchannel  $R$ -matrix calculations [18–20], we expect the same error in the final states as in the target states. At this point we remind the reader that the theoretical target state energies are used only to calculate short-range  $\bar{K}$  and  $\bar{D}$  parameters in Eq. (2) (the  $R$ -matrix part of the calculations), whereas experimental target state energies are used in the course of the MQDT calculations, when we impose boundary conditions in open and closed channels. Ionization thresholds and quantum defects are evaluated with experimental energies. Also, the use of experimental target energies and, in particular, the smooth behavior of the short-range parameters make the inclusion of relativistic effects adequate, in spite of the small magnitude of the target fine-structure splittings ( $< 0.1$  eV).

### C. Calculations of the initial and final states

Discretized outer-electron orbitals  $\varepsilon s$ ,  $\varepsilon p$ , and  $\varepsilon d$  are calculated inside the sphere of radius  $r_0$ , in a Hartree potential [20,32]

$$\left( -\frac{1}{2} \frac{d^2}{dr^2} + \frac{l(l+1)}{2r^2} - \frac{Z}{r} + V_H(r) \right) P_{nl}(r) = E_{nl} P_{nl}(r) + \sum_{n'} \lambda_{nn'} P_{n'l}(r),$$

$$V_H(r) = \sum_{n'} q_{n'l} \int_0^{r_0} \frac{1}{r_>} P_{n'l}^2(s) ds, \quad (5)$$

where  $r_>$  is the greater of the radial  $r$  and  $s$  coordinates,  $q_{n'l}$  are occupation numbers for the spectroscopic  $1s$ ,  $2s$ , and  $2p$  orbitals in the  $1s^22s^22p^5$  configuration. We use 12 closed-type orbitals that vanish at the  $R$ -matrix surface, and one open-type orbital, which has a nonzero amplitude at the surface and represents an outer electron escaping beyond  $r=r_0$  into an excited Rydberg state, or into a continuum. For brevity of notation, we use  $\varepsilon l$  to designate an electron in both open and closed MQDT channels (which in this sense have continuous energies), whereas  $nl$  is reserved strictly for discrete resonances.

To minimize the size of our expansion set, while keeping the most important configurations, we neglected all partial waves with angular momenta  $l > 2$ . Among those, the most important are  $f$  waves represented by the  $2p^4(^1D)3s(^2D)\varepsilon f^1P^o$  channel, which would reproduce the resonant  $4f$  state already identified by Codling *et al.* [2] at about 51.2 eV. An effect of  $f$  waves on other channels was tested and was found to be negligible in the photoionization. One can understand this by analyzing an interaction between  $2p^4(^1D)3s(^2D)\varepsilon f^1P^o$  and other doubly excited channels  $2p^43l\varepsilon l'$ . The interaction is represented by a matrix element of the Coulomb operator

$$\frac{1}{r_{ij}} = \sum_{k=0}^{\infty} \frac{r_{<}^k}{r_{>}^{k+1}} \mathbf{C}_i^{(k)} \cdot \mathbf{C}_j^{(k)}, \quad (6)$$

whose radial part is proportional to a Slater integral  $R^k(i,j;i',j')$  [33]. Among all channels, which contribute to the neon spectrum below 53 eV, only  $2p^43s\varepsilon p^1P^o$

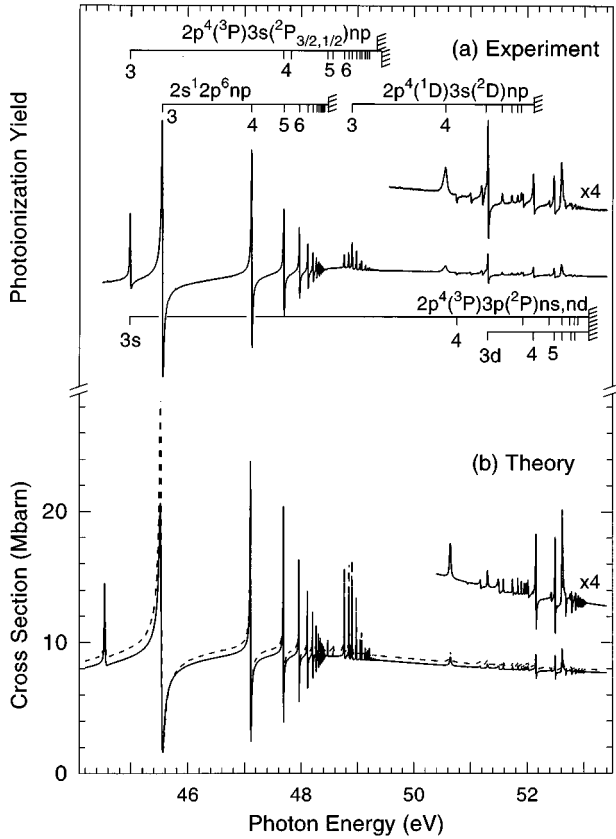


FIG. 3. (a) Experimental and (b) theoretical photoionization spectrum of neon from the ground state, plotted as a function of photon energy from 44 to 53 eV. The calculated cross section has been convolved with a Gaussian weight function of width 3.5 meV. Solid and dashed lines in (b) are the length- and velocity-gauge cross sections, respectively.

can interact with  $2p^4(^1D)3s(^2D)\epsilon f^1P^o$ ; other channels are excluded through spin-angular coupling rules for the  $r_{ij}^{-1}$  operator. However, the  $\langle 2p^4 3s \epsilon p^1 P^o | r_{ij}^{-1} | 2p^4(^1D)3s(^2D)\epsilon f^1 P^o \rangle$  interaction is proportional to a  $R^2(2p, \epsilon p; 2p, \epsilon f)$  Slater integral (and a corresponding exchange  $R^2$  integral), which typically is much smaller than the  $R^0$  or  $R^1$  Slater integrals appearing in the matrix elements among other  $2p^4 3s \epsilon p$  and  $2p^4 3p \epsilon l$  ( $l = s, d$ ) channels. Therefore, interactions with  $f$  waves can be safely neglected.

The initial state  $2p^6 1S$  is represented as a superposition of the target states coupled with the closed-type orbitals  $\epsilon s$ ,  $\epsilon p$ , and  $\epsilon d$ . The dominant terms in the CI expansion are listed in Table II. Our ionization energy of  $2p^6 1S$  is 22.094 eV, which is 0.497 eV more than the experimental value of 21.597 eV (see Table I). This difference translates into an error of only 0.01 in the quantum defect. Final states, which in  $LS$  coupling are represented by the  $^1P_1^o$ ,  $^3S_1^o$ ,  $^3P_1^o$ , and  $^3D_1^o$  partial waves, are constructed from the target states, and closed and open  $\epsilon s$ ,  $\epsilon p$ , and  $\epsilon d$  orbitals.

Although a relatively large number of basis functions is used, convergence problems plague our calculations. This is clearly apparent in the few percent discrepancy (on the average) between length- and velocity-gauge cross sections [34] (see Fig. 3), and in the slow convergence of short-range

scattering parameters. The convergence problems derive partly from the large excitation energies of the physical  $\text{Ne}^+$  states and partly from their strong correlation. The slowest converging are the  $d$  waves, which is mainly due to the inclusion of the  $\bar{3}d$  correlation orbital. Because  $\bar{3}d$ , which is the lowest  $nd$  orbital included in the target state wavefunction expansion, is so different from a spectroscopic  $3d$  orbital (see Sec. IV B and Fig. 2), any satisfactory representation of, for example, a  $2p^4(^3P)3p(^2P)3d$  resonant state will require a large number of basis-type  $\epsilon d$  orbitals to compensate for this large difference. (Note that this problem is absent in the heavier rare-gas atoms because of the different nature of the  $3d$  orbital; see Sec. IV B). The other correlation orbitals  $\bar{4}s$  and  $\bar{4}p$  do not slow down the convergence rate so much, because we include spectroscopic  $3s$  and  $3p$  orbitals in the target state representation. These spectroscopic  $\text{Ne}^+$  orbitals also describe the  $2p^4 3s 3p$  configuration of neon fairly accurately.

## V. EXPERIMENTAL AND THEORETICAL SPECTRA

Figure 3 shows the experimental and the convolved theoretical spectrum (in the length- and velocity-gauge forms [34]) over the energy range 44–53 eV. The theoretical cross section has been preconvolved with a Gaussian weight function of width 3.5 meV (FWHM), using a method described in Ref. [35]. This cross section decreases monotonically between 44 and 53 eV, and the average background photoionization yield is about 9–10 Mb. It is in agreement with other theoretical calculations, which also report the cross section at the 10 Mb level [12–14]. Both the present and the earlier calculations agree also well with absolute cross section measurements by Chan *et al.* [8], who report the cross section between 8 and 9 Mb.

Different energy ranges in this figure illustrate different excitation mechanisms. The energy region between 44 and 48.5 eV is dominated by singly excited resonances  $2s^2 2p^6 np^1 P^o$ , which are weakly perturbed by the  $n = 3, 4$ , and 5 members of the first doubly excited Rydberg series  $2p^4(^3P)3s(^2P)np^1 P^o$ . Sec. V A describes this portion of the spectrum in detail. Higher members of the  $2p^4(^3P)3s(^2P)np$  series dominate the adjacent region between 48.5 and 49.5 eV. Because of a relatively large fine-structure splitting of the  $2p^4(^3P)3s^2 P$  target state of 75.9 meV, two Rydberg series  $np_{3/2}$  and  $np_{1/2}$  converging to the two  $j_c = \frac{3}{2}$  and  $j_c = \frac{1}{2}$  levels, can be distinguished in this portion of the spectrum. These normally weak features are greatly enhanced by an interaction with the lowest-lying  $3p$  member of the  $2p^4(^1D)3s(^2D)np^1 P^o$  series, as will be discussed in Sec. V B. Higher-lying members of the  $2p^4(^1D)3s(^2D)np^1 P^o$  series ( $n > 3$ ) and other doubly excited Rydberg series  $2p^4 3s np$  and  $2p^4 3p nl$  ( $l = s, d$ ) characterize the energy range above 50.5 eV. Most of the experimentally resolved resonances in this portion of the spectrum are nearly pure  $LS$ -coupled states. An exception are the  $2p^4(^3P)3p(^2P)nl$  resonances, whose relativistic features can be resolved for the  $n > 7$  members. Section V C analyzes these features in greater detail.

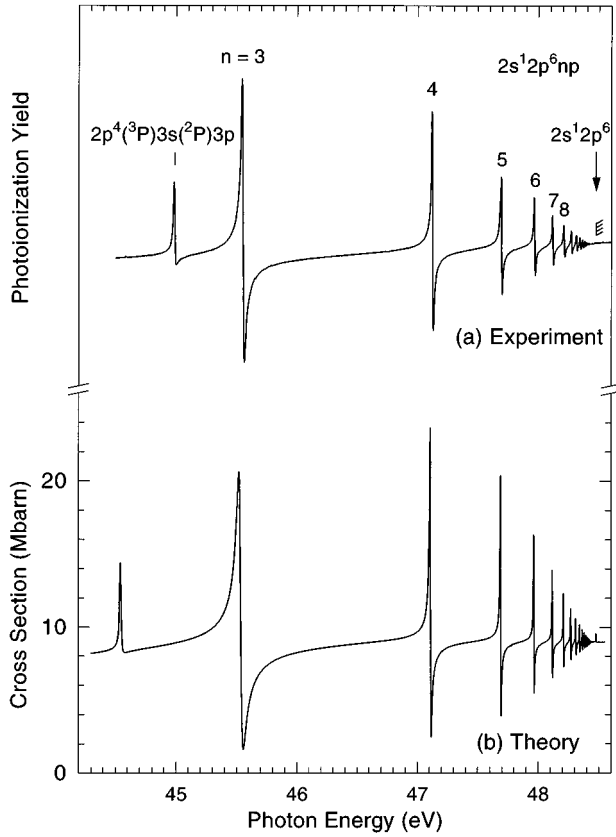


FIG. 4. (a) Experimental and (b) theoretical portion of the neon spectrum illustrating singly excited  $2s2p^6(^2S)np^1P^o$  Rydberg series and the first doubly excited  $2p^4(^3P)3s(^2P)3p$  state.

### A. Photon energy between 44 and 48.5 eV

Figure 4 shows a portion of the cross section in this energy range. In the upper panel, Fig. 4(a), the experimental spectrum and in the lower panel, Fig. 4(b), the calculated cross sections are shown. The spectrum is dominated by the  $2s2p^6(^2S)np^1P^o$  series, which is nearly unperturbed. At about 45.0 eV, the first double excitation resonance  $2p^4(^3P)3s3p^1P^o$  is seen, which is the common member of the Rydberg series  $2p^4(^3P)3s(^2P)np$  and  $2p^4(^3P)3p(^2P)ns$ . The  $2p^4(^3P)3s(^2P)4p$  and  $2p^4(^3P)3s(^2P)5p$  members fall also within this energy range, but are too weak to be seen on this scale. These resonances are discussed in more detail further below.

Table III lists experimental energies ( $E_r$ ) and effective quantum numbers ( $\nu$ ) from this work together with theoretical values from this work and experimental values from Codling *et al.* [2]. Additionally, Table III lists theoretical linewidths ( $\Gamma$ ) and corresponding reduced linewidths ( $\Gamma_{\text{red}} = \Gamma \nu^3$ ). Theoretical resonance parameters are calculated from the energy derivative of the eigenphase sum at its maximum, which is equivalent to the time-delay matrix,

$$\Gamma = 2 \left( \frac{d\delta}{dE} \right)_{E=E_r}^{-1}. \quad (7)$$

The phase-shift parametrization is independent of the experimental resolution, as opposed to the more standard parametrization of the Beutler-Fano profile [33]. For asymmetrical resonances, in particular for the  $2s2p^6np^1P^o$  series discussed here, the resonance position defined in Eq. (7) is approximately centered between the maximum and the minimum of the Beutler-Fano profile. However, the experimental

TABLE III. Resonance parameters of the  $2s2p^6(^2S)np^1P^o$  Rydberg series. The following theoretical and experimental values from this work and experimental values from Codling *et al.* [2] are listed: energy positions,  $E$  (eV), effective quantum numbers,  $\nu$ , linewidths,  $\Gamma$  (eV), and reduced linewidths,  $\Gamma_{\text{red}}$  (eV). The values in parentheses are experimental errors. The values in square brackets represent factors of powers of 10.

$n$	$E_{\text{th}}$	$E_{\text{exp}}$	$E_{\text{Ref.}[2]}$	$\nu_{\text{th}}$	$\nu_{\text{exp}}$	$\nu_{\text{Ref.}[2]}$	$\Gamma_{\text{th}}$	$\Gamma_{\text{red}}$
3	45.53397	45.5442(50)	45.547(9)	2.151	2.155(2)	2.155	0.349[-01]	0.347
4	47.11092	47.1193(50)	47.123(6)	3.158	3.168(6)	3.171	0.665[-02]	0.209
5	47.69182	47.6952(15)	47.694(6)	4.168	4.177(4)	4.17	0.247[-02]	0.179
6	47.96708	47.9650(30)	47.967(6)	5.176	5.17(2)	5.17	0.128[-02]	0.178
7	48.11856	48.1168(20)	48.116(6)	6.178	6.16(2)	6.15	0.729[-03]	0.172
8	48.21106	48.2093(20)	48.207(6)	7.181	7.16(3)	7.12	0.458[-03]	0.169
9	48.27170	48.2693(20)	48.271(6)	8.181	8.13(4)	8.16	0.307[-03]	0.168
10	48.31359	48.3124(10)	48.312(6)	9.181	9.15(3)	9.13	0.216[-03]	0.167
11	48.34375	48.3424(10)	48.344(6)	10.182	10.13(4)	10.18	0.158[-03]	0.167
12	48.36617	48.3650(10)	48.365(6)	11.182	11.12(5)	11.10	0.119[-03]	0.167
13	48.38331	48.3820(10)		12.182	12.10(7)		0.926[-04]	0.167
14	48.39669	48.3954(10)		13.182	13.07(8)		0.730[-04]	0.167
15	48.40734	48.4060(10)		14.182	14.04(10)		0.597[-04]	0.170
16	48.41596	48.4147(10)		15.182	15.02(12)		0.484[-04]	0.172
17	48.42303	48.4220(10)		16.182	16.02(15)		0.406[-04]	0.172
18	48.42890	48.4280(10)		17.182	17.01(18)		0.338[-04]	0.174
19	48.43383	48.4326(10)		18.181	17.91(21)		0.290[-04]	0.179
20	48.43801	48.4370(10)		19.181	18.92(25)		0.253[-04]	0.193

energies are taken at the intensity maxima of the resonances, which for spectral lines with negative Fano  $q$  parameters are shifted towards lower energies as compared with the theoretical positions. This energy shift is about half the resonance width  $\Gamma/2$ , and it translates into a constant shift  $\Gamma_{\text{red}}/2\mathcal{R}$  in the effective quantum numbers, where  $\mathcal{R}$  is the Rydberg constant. From Table III we find that  $\Gamma_{\text{red}} \approx 0.17$  eV, which increases the experimental effective quantum numbers by about 0.003. These differences between peak maxima and resonance energies, together with calibration errors, are considered in the experimental error bars.

Our experimental linewidth of the  $2s2p^63p$  state ( $\Gamma = 16 \pm 2$  meV) is comparable with the measured value  $\Gamma = 13 \pm 2$  meV of Codling *et al.* [2]. Our reduced linewidth ( $\Gamma_{\text{red}} = 0.16 \pm 0.02$  eV) is approximately constant for the whole series. However, our calculated width for  $2s2p^63p$  ( $\Gamma = 34$  meV) is larger than the observed one. Its calculated width and the width of the next  $2s2p^64p$  state ( $\Gamma = 6.6$  meV) is also larger than calculated by Burke and Taylor [12], 17 and 4 meV, respectively, and by Stener *et al.* [14], 13.9 and 3.9 meV, respectively. Differences in our calculated and measured quantum defects are, on the average, 0.04, well within the range of errors expected for such a strongly correlated target state. The experimental errors increase close to the ionization threshold, since small errors in energy trans-

late then into large errors in quantum defect. For better determination of the quantum defect of this nearly unperturbed series, we performed an additional fit of our experimental spectrum for the Rydberg series with constant quantum defects, including the states from  $n = 10$  to  $n = 19$ , and we got the new quantum defect  $\mu = 0.818 \pm 0.002$ , which compares well with the calculated value of 0.818. Our calculated effective quantum numbers for the  $2s2p^63p^1P^o$  ( $\nu = 2.151$ ) and  $2s2p^64p^1P^o$  ( $\nu = 3.158$ ) resonances are also comparable with earlier theoretical results of Burke and Taylor [12], who report their effective quantum numbers 2.176 and 3.192, respectively. Similar values of 2.184 and 3.208, respectively, were obtained by Hibbert and Scott [13]. The present and these earlier calculations predict, in this energy regime, nearly the same absolute cross sections of about 10 Mb.

The lowest resonance in this energy range, which is also the lowest resonance appearing in the neon spectrum above the first ionization threshold  $2p^5^2P$ , is a common member of the  $2p^4(^3P)3s(^2P)np^1P^o$  and  $2p^4(^3P)3p(^2P)ns^1P^o$  se-

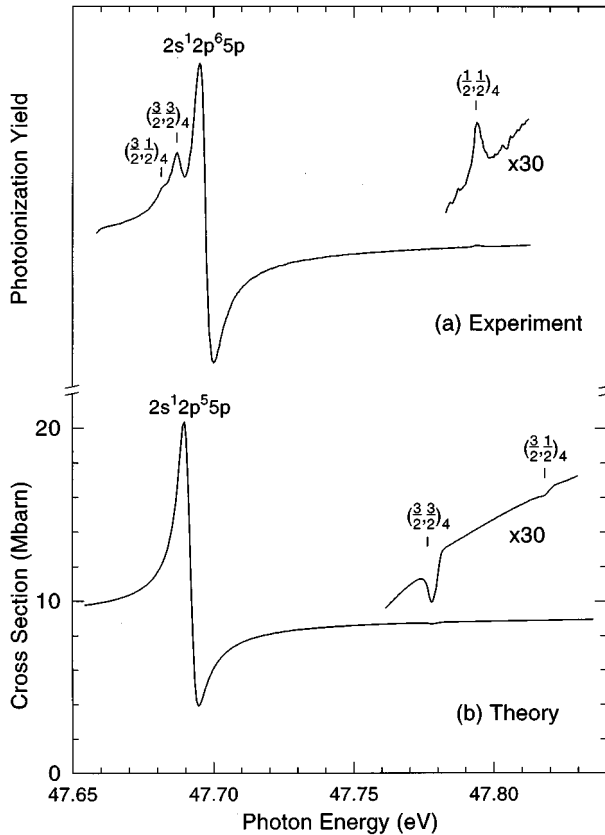


FIG. 5. Interference between  $2s2p^65p$  and  $2p^4(^3P)3s(^2P_{j_c})4p_{j_o}$  resonances in (a) the experimental and (b) the theoretical photoionization spectrum of neon. The doubly excited resonances are described in the relativistic  $jj$ -coupling scheme; here and in the other figures, we use a shorthand notation  $(j_c, j_o)_n$ , where  $j_c$  and  $j_o$  are total momenta of the core and of the outer electron, respectively.

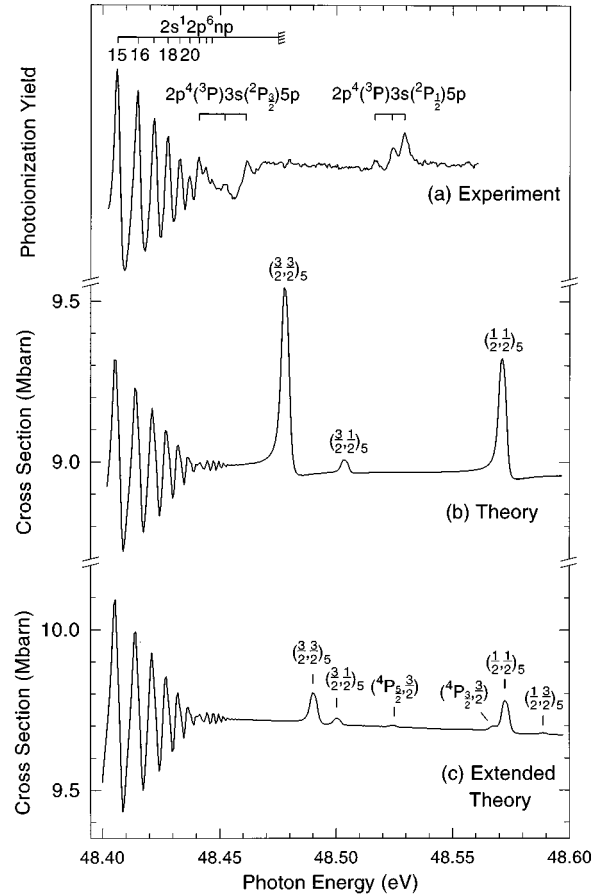


FIG. 6. The cross section in the vicinity of the  $2s2p^6^2S$  ionization threshold. The experimental spectrum (a) exhibits three perturbors just below  $2s2p^6^2S$ , and three peaks above it. The calculated cross section (b) reveals only four resonances, which are associated with the  $2p^4(^3P)3s^2P_{j_c}$  fine-structure levels of  $\text{Ne}^+$  and which are classified in  $jj$  coupling. Two additional resonances, which are associated with the  $(^4P_{j_c}, j_o)_n$  Rydberg series, show up in (c) if we extend our MQDT calculations to include  $2p^4(^3P)3s(^4P_{j_c})\epsilon p_{j_o}$  channels.

TABLE IV. Resonance parameters of the  $2p^4(^3P)3s(^2P_{j_c})np_{j_o}^1P^o$  Rydberg series. The resonances are classified corresponding to  $jj$ -coupling as  $(j_c, j_o)_n$ , analogous to Figs. 5–7. For  $n=5$ , no experimental values are given due to difficulties in assignment (see Fig. 6). The values in square brackets represent factors of powers of 10.

$(j_c, j_o)_n$	$E_{\text{th}}$	$E_{\text{exp}}$	$E_{\text{Ref.}[2]}$	$\nu_{\text{th}}$	$\nu_{\text{exp}}$	$\nu_{\text{Ref.}[2]}$	$\Gamma$	$\Gamma_{\text{red}}$
$n=3$	44.58283	44.9817(50)	44.980(8)	1.685	1.7602(10)	1.765	0.145[-01]	0.070
$(\frac{3}{2}, \frac{3}{2})_4$	47.78293	47.6870(15)		2.949	2.8622(13)		0.424[-03]	0.011
$(\frac{3}{2}, \frac{1}{2})_4$	47.82050	47.6817(15)		2.985	2.8576(13)		0.519[-03]	0.014
$(\frac{1}{2}, \frac{1}{2})_4$		47.7941(15)			2.8894(13)			
$(\frac{3}{2}, \frac{3}{2})_5$	48.47859			3.957			0.832[-03]	0.052
$(\frac{3}{2}, \frac{1}{2})_5$	48.50420			4.017			0.146[-03]	0.009
$(\frac{1}{2}, \frac{1}{2})_5$	48.57195		48.543(6)	3.998		3.930	0.492[-03]	0.031
$(\frac{1}{2}, \frac{3}{2})_5$	48.57782			4.011			0.330[-03]	0.025
$(\frac{3}{2}, \frac{3}{2})_6$	48.77197	48.7638(10)	48.763(6)	4.863	4.827(4)	4.82	0.437[-02]	0.416
$(\frac{3}{2}, \frac{1}{2})_6$	48.80917	48.7842(10)		5.028	4.913(4)		0.872[-04]	0.011
$(\frac{1}{2}, \frac{1}{2})_6$	48.85547	48.8422(10)	48.845(6)	4.895	4.837(4)	4.85	0.460[-02]	0.539
$(\frac{1}{2}, \frac{3}{2})_6$	48.88318			5.019			0.152[-03]	0.019
$(\frac{3}{2}, \frac{1}{2})_7$	48.97309	48.9586(10)		6.029	5.913(8)		0.868[-04]	0.019
$(\frac{3}{2}, \frac{3}{2})_7$	48.98279	48.9812(10)	48.982(6)	6.109	6.092(8)	6.10	0.173[-02]	0.394
$(\frac{1}{2}, \frac{3}{2})_7$	49.04784			6.019			0.782[-04]	0.017
$(\frac{1}{2}, \frac{1}{2})_7$	49.05161	49.0404(10)	49.042(6)	6.050	5.958(8)	5.97	0.421[-03]	0.131
$(\frac{3}{2}, \frac{1}{2})_8$	49.07245	49.0646(15)		7.035	6.93(2)		0.751[-04]	0.026
$(\frac{3}{2}, \frac{3}{2})_8$	49.07580	49.0742(10)	49.077(6)	7.078	7.052(12)	7.03	0.549[-03]	0.195
$(\frac{3}{2}, \frac{1}{2})_9$	49.13612			8.025			0.407[-04]	0.021
$(\frac{3}{2}, \frac{3}{2})_9$	49.13827	49.1343(10)	49.136(6)	8.067	7.98(2)	8.00	0.184[-03]	0.097
$(\frac{1}{2}, \frac{3}{2})_8$	49.14760			7.025			0.503[-04]	0.017
$(\frac{1}{2}, \frac{1}{2})_8$	49.14952	49.1448(10)	49.145(6)	7.050	6.984(12)	6.98	0.221[-03]	0.077
$(\frac{3}{2}, \frac{1}{2})_{10}$	49.18058			9.032			0.392[-04]	0.029
$(\frac{3}{2}, \frac{3}{2})_{10}$	49.18178	49.1803(10)	49.177(6)	9.065	9.01(3)	8.90	0.116[-03]	0.086
$(\frac{1}{2}, \frac{3}{2})_9$	49.21128			8.011			0.156[-04]	0.008
$(\frac{1}{2}, \frac{1}{2})_9$	49.21223	49.2078(15)	49.210(6)	8.029	7.94(3)	7.96	0.407[-04]	0.021
$(\frac{3}{2}, \frac{3}{2})_{11}$	49.21313	49.2133(10)		10.068	10.06(4)		0.578[-04]	0.059
$(\frac{3}{2}, \frac{1}{2})_{11}$	49.21368			10.088			0.123[-03]	0.126
$(\frac{3}{2}, \frac{3}{2})_{12}$	49.23558	49.2358(10)		11.032	11.02(5)		0.227[-04]	0.014
$(\frac{3}{2}, \frac{1}{2})_{12}$	49.23618			11.062			0.486[-04]	0.066
$(\frac{3}{2}, \frac{3}{2})_{13}$	49.25327	49.2548(10)		12.025	12.10(7)		0.112[-04]	0.019
$(\frac{3}{2}, \frac{1}{2})_{13}$	49.25382			12.061			0.359[-04]	0.063
$(\frac{1}{2}, \frac{3}{2})_{10}$	49.25636			9.028			0.234[-04]	0.017
$(\frac{1}{2}, \frac{1}{2})_{10}$	49.25705	49.2548(10)		9.047	8.98(3)		0.676[-04]	0.050
$(\frac{3}{2}, \frac{3}{2})_{14}$	49.26728	49.2678(10)		13.034	13.04(8)		0.148[-04]	0.033
$(\frac{3}{2}, \frac{1}{2})_{14}$	49.26761			13.062			0.251[-04]	0.056
$(\frac{3}{2}, \frac{3}{2})_{15}$	49.27826	49.2785(10)		14.032	14.01(10)		0.100[-04]	0.028
$(\frac{3}{2}, \frac{1}{2})_{15}$	49.27855			14.061			0.198[-04]	0.055
$(\frac{3}{2}, \frac{3}{2})_{16}$	49.28704	49.2878(10)		15.018	15.06(13)		0.410[-05]	0.014
$(\frac{3}{2}, \frac{1}{2})_{16}$	49.28736			15.058			0.178[-04]	0.061
$(\frac{1}{2}, \frac{3}{2})_{11}$	49.28805			10.030			0.177[-04]	0.018

TABLE IV (Cont.)

$(j_c, j_o)_n$	$E_{\text{th}}$	$E_{\text{exp}}$	$E_{\text{Ref.}[2]}$	$\nu_{\text{th}}$	$\nu_{\text{exp}}$	$\nu_{\text{Ref.}[2]}$	$\Gamma$	$\Gamma_{\text{red}}$
$(\frac{1}{2}, \frac{1}{2})_{11}$	49.28852	49.2878(10)		10.048	10.01(4)		0.440[-04]	0.045
$(\frac{3}{2}, \frac{3}{2})_{17}$		49.2950(10)			16.05(16)			
$(\frac{3}{2}, \frac{3}{2})_{18}$		49.3013(10)			17.11(18)			
$(\frac{1}{2}, \frac{1}{2})_{12}$		49.3108(10)			10.98(5)			
$(\frac{1}{2}, \frac{1}{2})_{13}$		49.3288(10)			11.97(6)			
$(\frac{1}{2}, \frac{1}{2})_{14}$		49.3428(10)			12.97(8)			
$(\frac{1}{2}, \frac{1}{2})_{15}$		49.3538(10)			13.95(10)			
$(\frac{1}{2}, \frac{1}{2})_{16}$		49.3633(10)			15.01(12)			
$(\frac{1}{2}, \frac{1}{2})_{17}$		49.3703(10)			15.96(15)			
$(\frac{1}{2}, \frac{1}{2})_{18}$		49.3768(10)			17.03(18)			

ries. However, its eigenvector composition and its effective quantum number definitely favors the membership in the  $2p^4(^3P)3s(^2P)np^1P^o$  series. Its experimental quantum defect  $\mu$  is 1.24, which is much more than the quantum defects ( $\cong 1.0$ ) of higher members of these series (see Table IV). Its larger quantum defect can be attributed to the confinement of the  $3s3p$  radial wave function in the reaction zone, which, in turn, enhances the electron correlation. Therefore, the dynamics of this state are dominated mainly by short-range forces, as opposed to higher-lying members, where long-range forces play the dominant role. Apart from the difference in the quantum defect, the  $3s3p$  member appears in the spectrum to be much more intense than the  $3s4p$  and  $3s5p$  members. As pointed out in Sec. IIB, the doubly excited resonances are photoexcited to the extent of correlation in the ground state. Due to the major contribution of the  $2p^5(^2P)3p^1S$  correlation configuration in the ground state, all  $2p^43s3p$  resonances can be photoexcited. However, the higher-lying  $np$  resonances ( $n > 3$ ) can only be reached from the ground state due to the presence of other initial state configurations and therefore appear much weaker in the photoionization cross section. Indeed, the  $2p^4(^3P)3s(^2P)4p^1P^o$  resonance is comparatively very weak, and was not even resolved in the earlier photoabsorption spectrum [2,3].

At present, we identified the  $3s4p$  resonant state as a weak perturbation in the spectrum in the vicinity of the  $2s2p^65p^1P^o$  resonance; Fig. 5 magnifies this portion of the spectrum. Close to this resonance, weak features are visible, which are resolved here. The additional peaks belong to the  $4p$  members of the  $2p^4(^3P)3s(^2P_{j_c})np_{j_o}^1P^o$  series. This series is no longer pure in  $LS$  coupling but is split into four resonances, which are classified within the  $jj$ -coupling scheme  $(j_c, j_o)_n$ . Features with  $j_c = \frac{3}{2}$  and  $j_c = \frac{1}{2}$  are measured at  $\cong 47.68$  eV and 47.80 eV, respectively. We observe the  $(\frac{3}{2}, \frac{3}{2})_4$  resonance on the lower energy side of the  $2s2p^55p$ , with the  $(\frac{3}{2}, \frac{1}{2})_4$  resonance as a weak shoulder. The  $(\frac{3}{2}, \frac{3}{2})_4$  and  $(\frac{3}{2}, \frac{1}{2})_4$  are greatly enhanced by interaction with the  $2s2p^55p$  resonance, while the  $(\frac{1}{2}, \frac{1}{2})_4$  resonance at  $\cong 47.80$  eV is found to be very weak, and the  $(\frac{1}{2}, \frac{3}{2})_4$  state is not visible.

Our theoretical calculations fail, however, to reproduce these features with a comparable accuracy. This difficulty can be understood if one analyzes the mixing,  $|c_k|^2$ , between two weakly interacting configurations, which is given in first-order perturbation theory by

$$|c_k|^2 \cong \left| \frac{\langle \Psi_o | H | \Psi_k \rangle}{E_o - E_k} \right|^2. \quad (8)$$

For weakly interacting and nearly degenerate levels,  $|c_k|^2$  is very sensitive to the zero-order energy separation  $E_o - E_k$ , and even an error of 0.02 in quantum defects completely destroys this interference pattern.

At higher energies, six additional resonances are visible, some of which straddle the ionization threshold  $2s2p^62S$ . With our good resolution and signal-to-noise ratio, it is now possible to resolve these perturbing features and the  $2s2p^6np^1P^o$  series up to  $n > 20$ . Figure 6 shows a magnification of the high-energy part of the  $2s2p^6np$  series ( $n > 15$ ) as well as additional resonances converging to the next ionization threshold. Codling *et al.* [2] observed only one resonance at 48.543 eV and classified it as  $2p^4(^3P)3s(^2P_{1/2})5p^1P^o$ . In addition, we observe the  $2p^4(^3P)3s(^2P_{3/2})5p^1P^o$  and other very weak resonances. However, their identification is difficult, because even a small error in their theoretical positions (which is about 0.02 in the quantum defect) drastically changes this portion of the neon spectrum. Furthermore, the occurrence of six resonances found in the experiment could not be explained easily, as there can be only four  $5p$  members associated with the  $2p^4(^3P)3s^2P_{j_c}$  thresholds. In the  $jj$ -coupling scheme, they are characterized as:  $(\frac{3}{2}, \frac{3}{2})_5$ ,  $(\frac{3}{2}, \frac{1}{2})_5$ ,  $(\frac{1}{2}, \frac{3}{2})_5$ ,  $(\frac{1}{2}, \frac{1}{2})_5$ . The origins of the other two peaks were identified through a smaller scale calculation that included in the target-state representation all doublet and quartet  $\text{Ne}^+$  states, which might contribute to resonances in this energy range. These extended calculations showed [see Fig. 6(c)] that the additional peaks are probably associated with members of the  $np$  Rydberg series converging to the  $j_c = \frac{3}{2}$  and  $j_c = \frac{5}{2}$  levels of the  $2p^4(^3P)3s^4P$  target state. Only tentative assignments, which specify the total momentum  $j_c$  of the target, but leave

out the total momentum  $j_o$  of the outer electron, could be made because of the large discrepancy between theory and experiment.

### B. Photon energies between 48.7 and 49.4 eV: A detailed study of the $2p^4(^1D)3s(^2D)3p^1P^o$ perturber

Figure 7 covers the photon-energy range between 48.7 and 49.4 eV. Three  $jj$ -coupled series  $2p^4(^3P)3s(^2P_{j_c})np_{j_o}$  can be seen:  $(j_c, j_o)_n = (\frac{3}{2}, \frac{3}{2})_n$ ,  $(\frac{1}{2}, \frac{1}{2})_n$ , and  $(\frac{3}{2}, \frac{1}{2})_n$ , all of which are perturbed by the  $2p^4(^1D)3s(^2D)3p^1P^o$  resonance; the  $(\frac{1}{2}, \frac{3}{2})_n$  series is too weak to be resolved. The  $(\frac{3}{2}, \frac{3}{2})_n$  and  $(\frac{1}{2}, \frac{1}{2})_n$  series are greatly enhanced and shifted in energy, while the  $(\frac{3}{2}, \frac{1}{2})_n$  series is only weakly perturbed. In addition, the  $(\frac{3}{2}, \frac{3}{2})_n$  and  $(\frac{1}{2}, \frac{1}{2})_n$  series perturb each other, as is evident at  $h\nu = 49.14$  eV, for example, where the intensity of the  $(\frac{3}{2}, \frac{3}{2})_9$  resonance is decreased and that of the  $(\frac{1}{2}, \frac{1}{2})_8$  resonance is increased. In addition to several resonances that were observed previously, many additional resonances are now resolved. The  $2p^4(^3P)3s(^2P_{3/2})np_{3/2}$  and  $2p^4(^3P)3s(^2P_{1/2})np_{1/2}$  are resolved up to  $n=18$ , and the  $2p^4(^3P)3s(^2P_{3/2})np_{1/2}$  series is identified up to  $n=8$ . The better spectral resolution of the present experiment, combined with the theoretical calculations, allows us to assign all resolved levels, and provide a complete and comprehensive picture of this strong interplay between correlation and relativistic effects.

Table IV shows the theoretical and experimental resonance parameters from this work together with experimental values from Codling *et al.* [2]. The experimental linewidth of the  $2p^43s(^2P_{1/2})3p$  state is  $\Gamma = 10 \pm 2$  meV, and it agrees well with that of Codling *et al.* [2], who measured  $\Gamma = 10 \pm 3$  meV. The linewidth of the higher members of the  $2p^4(^3P)3s(^2P_{j_c})np_{j_o}$  series are difficult to determine because their autoionization widths are comparable to, or less than, the monochromator resolution and because of saturation effects due to the rather high neon pressure in the gas cell that is needed for good signal-to-noise ratio. However, linewidths and transition strengths (intensities in the experimental spectra) are strongly correlated as in the case of helium [36]. In Fig. 7, a variation in intensities is seen, which correlates with the theoretical linewidth in Table IV. Agreement between theoretical and experimental quantum defects is, on the average, at the level of  $\Delta\mu \cong 0.02$ .

The resonances in Table IV are classified according to the  $jj$ -coupling scheme. We found for the majority of these resonances, that the eigenvectors are purer in  $jj$  coupling than in  $jk$  coupling. It is counterintuitive to the general trend in the rare-gas atoms, where  $jk$  coupling is usually better [37]. Higher-lying resonances in Table IV (for  $n > 12$ ) appear to be actually purer in  $jk$  coupling, but we retain the original  $jj$  notation for consistency.

Various perturbations found in this energy range derive from  $2p^4(^1D)3s(^2D)3p^1P^o$  and from interactions between the Rydberg series associated with the  $j_c = \frac{3}{2}$  and  $j_c = \frac{1}{2}$  fine-structure levels of the  $2p^4(^3P)3s^2P$  target. These latter perturbations occur nearly periodically in Figs. 8(a) and 8(b), where we plotted resonance quantum defects,  $\mu_{3/2} = n - \nu_{3/2}$ , and reduced linewidth,  $\Gamma_{\text{red}}$ , on the scale of

effective quantum numbers,  $\nu_{1/2}$ , associated with the  $j_c = \frac{1}{2}$  ionization threshold. This figure illustrates the effect of the  $2p^4(^1D)3s(^2D)3p^1P^o$  perturber and of the  $(\frac{1}{2}, j_o)_n$  resonances on the host spectrum of  $(\frac{3}{2}, j_o)_n$  autoionizing Rydberg series. The  $(\frac{3}{2}, \frac{3}{2})_n$  and  $(\frac{3}{2}, \frac{1}{2})_n$  Rydberg series are marked with full and empty diamonds ( $\diamond$ ), respectively, and the  $(\frac{1}{2}, \frac{1}{2})_n$  and  $(\frac{1}{2}, \frac{3}{2})_n$  series are marked with full and empty squares ( $\square$ ). The major perturber  $2p^4(^1D)3s(^2D)3p^1P^o$  is marked by a bullet ( $\bullet$ ). The quantum defects  $\mu_{3/2}$  (modulo 1) and the reduced widths  $\Gamma_{\text{red}} = \Gamma \nu_{3/2}^3$  are calculated, for all resonances, with respect to the  $j_c = \frac{3}{2}$  ionization threshold, using data from Table IV and a relation between Rydberg energies in two channels, namely,  $E_{3/2} - \mathcal{R}/\nu_{3/2}^2 = E_{1/2} - \mathcal{R}/\nu_{1/2}^2$ .

One can extract regularities in these perturbed  $(\frac{3}{2}, j_o)_n$  Rydberg series if the discrete points are connected by two sets of continuous curves. Then, all  $(\frac{3}{2}, \frac{3}{2})_n$  resonances (full diamonds) are located on one branch, and the  $(\frac{3}{2}, \frac{1}{2})_n$  resonances (empty diamonds) belong to the other branch of curves. The curves in Fig. 8(a), are equivalent to Lu-Fano plots familiar for bound spectra [38]. Here, for the autoionizing spectrum, we adopted a different formulation, which was earlier used to study perturbations in autoionizing Rydberg series in beryllium [39] and in aluminum [40]. The continuous curves connecting the discrete points are approximate solutions of a complex determinant in the MQDT formulation,

$$\det|\underline{S}^{cc} - e^{-2i\pi\nu}| = 0, \quad (9)$$

$$\underline{S} = \frac{1 + i\underline{K}}{1 - i\underline{K}}. \quad (10)$$

$\underline{S}^{cc}$  is a closed-closed portion of the short-range scattering matrix  $\underline{S}$ , and  $\underline{K}$  is the short-range reaction matrix used in Eq. (2). In standard calculations, Eq. (9) is used to find discrete positions and widths of resonances, which produces the same result as the solution of Eq. (7). Here we solve it approximately; we rewrite Eq. (9) into an eigenvalue equation and then enforce exponential decay in all closed channels of the submatrix  $\underline{S}^{cc}$ , except those attached to the lowest threshold  $2p^4(^3P)3s^2P_{3/2}$ ,

$$\underline{S}_a^{\text{red}} \mathbf{A}_a = e^{-2i\pi\nu_a} \mathbf{A}_a, \quad (11)$$

$$\underline{S}_a^{\text{red}} = \underline{S}_{aa} - \underline{S}_{ab}(\underline{S}_{bb} - e^{-2i\pi\nu_b})^{-1} \underline{S}_{ba}. \quad (12)$$

In the partitioned matrix  $\underline{S}^{cc}$ , the index ‘‘a’’ labels artificially opened  $(\frac{3}{2}, \frac{3}{2})$  and  $(\frac{3}{2}, \frac{1}{2})$  channels associated with the  $2p^4(^3P)3s^2P_{3/2}$  level, whereas the index ‘‘b’’ labels all other closed channels converging to the  $2p^4(^3P)3s^2P_{1/2}$  level and to higher-lying thresholds.  $\underline{S}_a^{\text{red}}$  is thus a two-by-two matrix, whose eigenvalues  $e^{-2i\pi\nu_a}$  describe the  $(\frac{3}{2}, \frac{3}{2})$  and  $(\frac{3}{2}, \frac{1}{2})$  channels. The real part ( $\text{Re}\mu_a$ ) and twice the imaginary part ( $2\text{Im}\mu_a$ ) of the complex quantum defects  $\mu_a = n - \nu_a$ , which are associated with those eigenvalues,

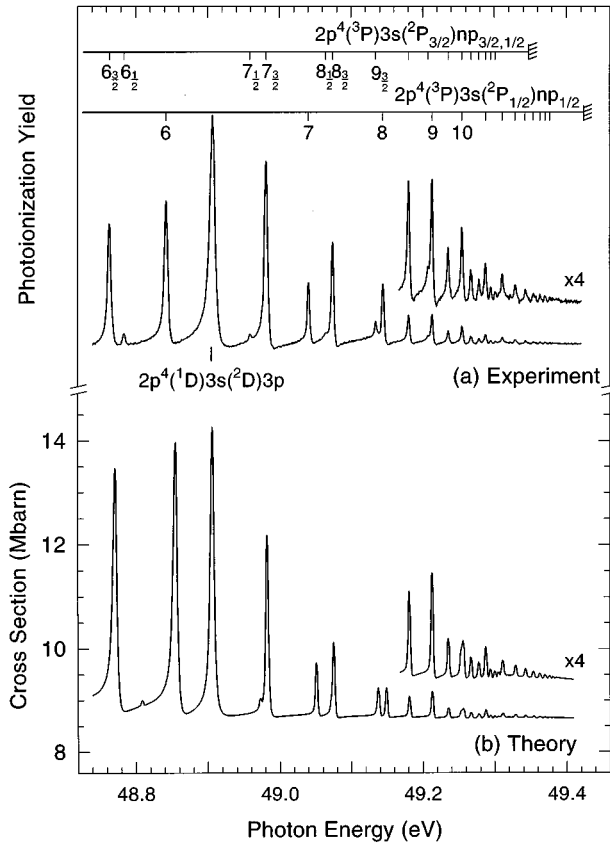


FIG. 7. (a) Experimental and (b) theoretical autoionizing Rydberg series  $2p^4(^3P)3s(^2P_{j_c})np_{j_o}$ , which overlap with the  $2p^4(^1D)3s(^2D)3p^1P^o$  perturber.  $j_c = \frac{3}{2}$  resonances,  $(\frac{3}{2}, j_o)_n$ , are represented as  $n_{j_o}$ .

are just the two continuous lines plotted in Fig. 8(a) and Fig. 8(b), respectively. They are related to Rydberg-state energies in a complex plane,

$$E = E_a - \frac{1}{2\nu^2} \cong E_a - \frac{1}{2(n - \text{Re}\mu_a)^2} - \frac{i}{2} \frac{2\text{Im}\mu_a}{(n - \text{Re}\mu_a)^3}, \quad (13)$$

where  $E_a$  (a.u.) is the  $j_c = \frac{3}{2}$  ionization threshold.

The solutions to Eq. (11) exhibit perturbers associated with the closed- $b$  channels, i.e.,  $(\frac{1}{2}, j_o)_n$  and  $2p^4(^1D)3s(^2D)3p^1P^o$  perturbers. The  $(\frac{1}{2}, j_o)_n$  perturbers appear nearly periodically in Fig. 8; every time a quantum defect in a  $(\frac{3}{2}, j_o)$  channel ( $\text{Re}\mu_a$ ) passes through this perturber, it is increased by one, analogously to a phase shift in a true continuum channel when it passes through a resonance. Effects of these perturbations on the physically observable resonances  $(\frac{3}{2}, j_o)_n$ , which are marked by diamonds, are most pronounced near  $\nu_{1/2} = 9$  and  $\nu_{1/2} = 10$ , where the quantum defects experience a small shift from their average values. The effect of the  $2p^4(^1D)3s(^2D)3p^1P^o$  perturber can be traced over several  $(\frac{1}{2}, j_o)_n$  resonances, as it slowly increases the  $\text{Re}\mu_a$  quantum defects. Nearly periodical perturbers are observed also for the reduced widths  $2\text{Im}\mu_a$  in Fig. 8(b). Here, in addition, we find that the

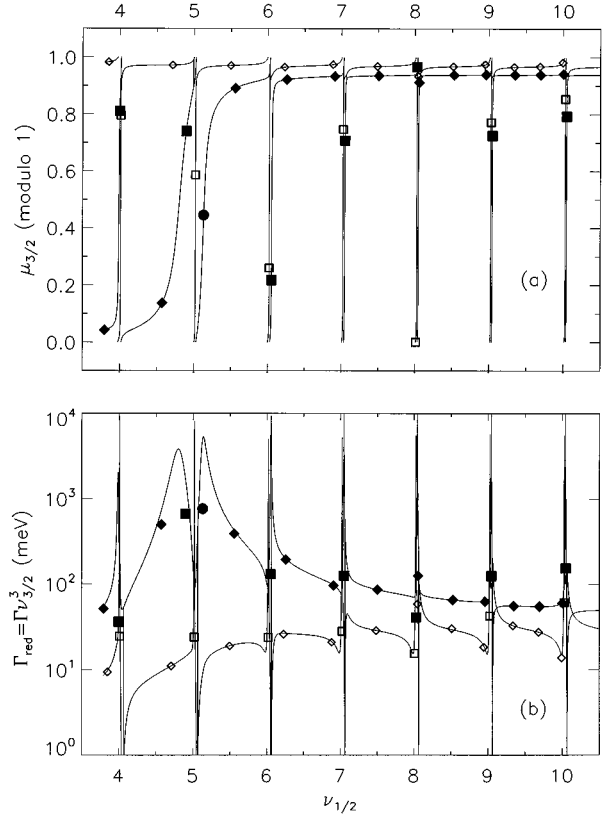


FIG. 8. Perturbations and regularities in the  $2p^4(^3P)3s(^2P_{j_c})np_{j_o}$  autoionizing Rydberg series, as plotted on the scale of effective quantum numbers  $\nu_{1/2}$  associated with the  $2p^4(^3P)3s^2P_{1/2}$  threshold. Full and empty diamonds ( $\diamond$ ) mark quantum defects  $\mu$  (a) and the reduced widths  $\Gamma_{red} = \Gamma \nu_{3/2}^3$  (b) of the  $(\frac{3}{2}, \frac{3}{2})_n$  and  $(\frac{3}{2}, \frac{1}{2})_n$  Rydberg series, respectively, and full and empty squares ( $\square$ ) mark the  $(\frac{1}{2}, \frac{1}{2})_n$  and  $(\frac{1}{2}, \frac{3}{2})_n$  Rydberg series. We use the shorthand notation  $(j_c, j_o)_n$ , as in Fig. 5. The broad perturber  $2p^4(^3P)3s(^2P)3p^1P^o$  is indicated by a bullet ( $\bullet$ ). These discrete resonance parameters are directly calculated from data in Table IV, by equating energies of Rydberg states converging to  $j_c = \frac{3}{2}$  and  $j_c = \frac{1}{2}$  thresholds, i.e.,  $E_{3/2} - \mathcal{R}/\nu_{3/2}^2 = E_{1/2} - \mathcal{R}/\nu_{1/2}^2$ . These data are found to lie near approximative, but continuous and nearly periodical curves, which are solutions to Eq. (10).

$2p^4(^1D)3s(^2D)3p^1P^o$  perturber increases reduced widths of  $(\frac{3}{2}, \frac{3}{2})_n$  and  $(\frac{1}{2}, \frac{1}{2})_n$  resonances (marked by filled diamonds and squares), as they overlap with the upper branch of  $2\text{Im}\mu_a$ , and at the same time it strongly decreases (on the average by an order of magnitude) the reduced widths of the other two series  $(\frac{3}{2}, \frac{1}{2})_n$  and  $(\frac{1}{2}, \frac{3}{2})_n$  (marked by empty points), as they overlap with the lower branch of  $2\text{Im}\mu_a$ . This, in part, explains why resonances with quantum numbers  $j_o = j_c$  are enhanced in the spectrum, whereas the other group of much narrower resonances  $j_o \neq j_c$  is barely resolved; note that  $(\frac{3}{2}, \frac{3}{2})_n$  and  $(\frac{1}{2}, \frac{1}{2})_n$  are the dominant resonances in Fig. 7, and they also appear strong in Fig. 3. Of course, this enhancement in the photoionization cross section is also, in part, due to correlation in the initial state, which allows for a dipole transition between the  $2p^5(^2P)3p^1S$  initial-state configuration and the  $2p^4(^1D)3s(^2D)3p^1P^o$  state (see Sec. II B), and partly due to correlation among the doubly excited Rydberg states.

In the following, we explain, using simple arguments, why the interaction between the broad perturber and the  $j_o = j_c$  series is much stronger than between the perturber and the  $j_o \neq j_c$  series. For a qualitative explanation we assume that the interaction is mainly due to Coulomb forces, whereas the target fine-structure splitting amounts to a simple geometric rotation of the channel functions from  $LS$ - to  $jj$ -coupling. The relative interaction between the  $(j_c, j_o)$  channels, explicitly  $2p^4(^3P)3s(^2P_{j_c})\epsilon p_{j_o}$ , and the perturber, which is nearly a pure  $1P^o$  state in the  $LS$ -coupled representation, is proportional to the square of recoupling coefficients connecting the  $LS$ -coupled function  $2p^4(^3P)3s(^2P)\epsilon p^1P^o$  and the  $jj$ -coupled functions  $2p^4(^3P)3s(^2P_{j_c})\epsilon p_{j_o}$ . The square of the recoupling coefficients for the  $(\frac{3}{2}, \frac{3}{2})_n$ ,  $(\frac{3}{2}, \frac{1}{2})_n$ ,  $(\frac{1}{2}, \frac{3}{2})_n$ , and  $(\frac{1}{2}, \frac{1}{2})_n$   $jj$ -coupled functions scales as 5:1:1:2, respectively, which explains the different perturbation of the different  $jj$  channels, and consequently the enhancement of the  $(\frac{3}{2}, \frac{3}{2})_n$  and  $(\frac{1}{2}, \frac{1}{2})_n$  Rydberg series in the cross section.

The same mechanism is also responsible for an exchange of relative positions between the  $(\frac{3}{2}, \frac{3}{2})_n$  and  $(\frac{3}{2}, \frac{1}{2})_n$  members, and between the  $(\frac{1}{2}, \frac{1}{2})_n$  and  $(\frac{1}{2}, \frac{3}{2})_n$  members. This exchange takes place in Fig. 8(a) between  $\nu_{1/2} = 4.5$  and  $\nu_{1/2} = 5.5$  (see also the exchange between the  $n=6$  and  $n=7$  resonances in Table IV and Fig. 7).

### C. Photon energies between 50 and 53 eV

This portion of the experimental spectrum is shown in Fig. 9, together with the theoretical cross section. Resonance parameters are given in Tables V–VII. The portion of the spectrum in Fig. 9 is characterized by overlapping, doubly excited resonances  $2p^4(^1D)3s(^2D)np^1P^o$  and  $2p^4(^3P)3p(^2P)nl^1P^o$  ( $l=s, d$ ). In addition, the  $2p^4(^3P)3p(^2D)3s^1P^o$  and  $2p^4(^1D)3s(^2D)4f^1P^o$  resonances, and a low-lying  $3s3p$  perturber associated with the  $2p^4(^1S)3s^2S$  ionization threshold show up.

Our designation of the  $2p^4(^3P)3p(^2P)4s^1P^o$ ,  $2p^4(^3P)3p(^2D)3d^1P^o$ , and  $2p^4(^1D)3s(^2D)4f$  resonances between 50.7 and 51.2 eV is only tentative and is based on the earlier studies [2]. In this classification, the quantum defect of the  $2p^4(^3P)3p(^2P)4s^1P^o$  resonance is  $\mu = 1.577(3)$  and it fits very well within the values of the upper members, which have  $\mu \approx 1.55$ . On the other hand, the line shape and the theoretical calculations favor an exchange of the classification of  $2p^4(^3P)3p(^2P)4s^1P^o$  and  $2p^4(^3P)3p(^2D)3d^1P^o$ . Our calculations do not unambiguously reproduce experimental features characteristic of these levels, although at the same time they nearly accurately reproduce results in other portions of the spectrum. For example, the positions of the two resonances appear in a different order in experiment and in theory. Moreover, the  $4f$  resonance has not been included in the calculations.

The first resonance in this energy range, situated at 50.5 eV, is the  $3s4p$  member of the  $2p^4(^1D)3s(^2D)np^1P^o$  Rydberg series. It appears to be much broader than the  $3s3p$  member, which is at 48.9 eV (see Sec. V B), counterintuitive to the scaling rule  $\Gamma \propto \nu^{-3}$ . Codling *et al.* [2] pointed out that this resonance broadening is caused by a strong interaction between  $2p^4(^1D)3s(^2D)\epsilon p^1P^o$  and the

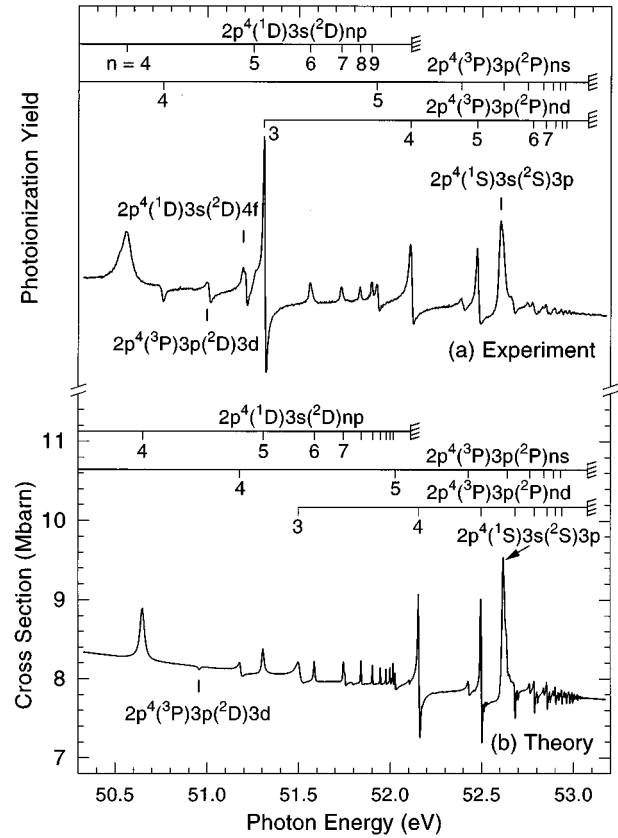


FIG. 9. (a) Experimental and (b) theoretical photoionization spectrum between 50.4 and 53.2 eV. This region is dominated by overlapping  $2p^43snp$  and  $2p^43pnl$  ( $l=s, d$ ) Rydberg series.

$2p^4(^3P)3s(^2P)\epsilon p^1P^o$  channel, which opens up at 49.4 eV, thus above the first  $3s3p$  member. From Table V we find that the reduced width of  $3s4p$  is an order of magnitude larger than that of  $3s3p$ . To verify Codling's finding we estimated partial reduced widths of  $3snp$  resonances, with respect to the  $2p^4(^3P)3s(^2P)\epsilon p^1P^o$  continuum (for  $n > 3$ ) and with respect to the other available continua  $2p^5\epsilon l^1P^o$  ( $l=s, d$ ) and  $2s2p^6\epsilon p^1P^o$  (for  $n \geq 3$ ). A partial reduced width is approximately  $|S_{co}|^2$ , where  $S_{co}$  is an element of a short-range scattering matrix [Eq. (10)] connecting closed and open channels. We found that a sum of partial reduced widths for autoionization into  $2p^5\epsilon l^1P^o$  ( $l=s, d$ ) and  $2s2p^6\epsilon p^1P^o$  channels, is about 0.01–0.02 a.u., whereas the partial reduced width for autoionization into  $2p^4(^3P)3s(^2P)\epsilon p^1P^o$  is, on an average, 0.1 a.u., which explains the broadening of the  $3snp$  ( $n > 3$ ) resonances as compared with the  $3s3p$  resonance.

Higher members of the  $2p^4(^1D)3s(^2D)np^1P^o$  series ( $n > 5$ ) also decay predominantly into the  $2p^4(^3P)3s(^2P)\epsilon p^1P^o$  continuum, although their decay is more complicated owing to interference with other perturbers converging to higher-lying ionization thresholds. A prominent example is a perturbation arising from the  $2p^4(^3P)3p(^2P)5s^1P^o$  resonance near 52 eV. A magnification of this energy region is shown in Fig. 10. All  $3snp$  resonances below the  $3p5s$  perturber have high intensities, whereas members above  $3p5s$  are strongly suppressed in the photoionization spectrum. In theory, the energy of the per-

TABLE V. Resonance parameters of the  $2p^4(^1D)3s(^2D)np\ ^1P^o$  Rydberg series. Experimental and theoretical values from this work and experimental values from Codling *et al.* [2] are listed.

$n$	$E_{\text{th}}$	$E_{\text{exp}}$	$E_{\text{Ref.}[2]}$	$\nu_{\text{th}}$	$\nu_{\text{exp}}$	$\nu_{\text{Ref.}[2]}$	$\Gamma_{\text{th}}$	$\Gamma_{\text{red}}$
3	48.90635	48.9066(15)	48.907(7)	2.060	2.0597(5)	2.060	0.449[-02]	0.039
4	50.64958	50.5600(70)	50.565(20)	3.049	2.959(7)	2.963	0.276[-01]	0.781
5	51.30491	51.2620(50)	51.276(20)	4.102	3.997(12)	4.03	0.137[-01]	0.945
6	51.58653	51.5610(30)	51.563(7)	5.082	4.961(13)	4.97	0.686[-02]	0.901
7	51.74499	51.7320(30)	51.736(7)	6.078	5.970(23)	5.99	0.384[-02]	0.863
8	51.84188	51.8332(15)	51.842(7)	7.080	6.964(19)	7.06	0.147[-02]	0.520
9	51.90467	51.8975(15)	51.898(20)	8.075	7.933(28)	7.93	0.975[-03]	0.513
10	51.94790			9.069			0.600[-03]	0.447
11	51.97886	51.9792(25)		10.059	10.058(93)		0.338[-03]	0.344
12	52.00167	52.0032(25)		11.039	11.10(13)		0.155[-03]	0.209
13	52.01858	52.0208(25)		11.985	12.10(16)		0.189[-03]	0.325
14	52.02989	52.0348(25)		12.771	13.13(21)		0.200[-02]	4.163
15		52.0452(25)			14.09(26)			
16		52.0542(25)			15.12(32)			

turbur is overestimated by about 0.1 eV, and only  $n > 13$  Rydberg series members are suppressed in the spectrum. An additional perturbation of the  $2p^4(^1D)3s(^2D)np\ ^1P^o$  series arises from the  $2p^4(^3P)3p(^2P)4d\ ^1P^o$  state, which straddles the  $2p^4(^1D)3s\ ^2D$  ionization threshold.

This portion of the calculated spectrum also exhibits very weak  $3p4d$  and  $3p5d$  resonances associated with the  $2p^4(^3P)3p\ ^2D$  threshold, although they are too weak to be resolved in the experimental spectrum (see also discussion in Sec. II B); the only experimentally resolved member of this series is  $3p3d$  at about 51.0 eV. Although relativistic features are expected to be strong for this Rydberg series (owing to the large target state fine-structure splitting of 63.3 meV), no attempt has been made to classify these resonances according a particular  $(j_c, j_o)_n$  or  $[j_c, np]K$  coupling scheme.

The spectrum above 52.5 eV, shown in Fig. 11, is dominated by the  $2p^4(^3P)3p(^2P)nl$  ( $l=s, d$ ) Rydberg series and a low-lying  $2p^4(^1S)3s(^2S)3p$  perturber. In the calculations, we adjusted the perturber's position to match the experimental spectrum in Fig. 11(a), by shifting the  $2p^4(^1S)3s\ ^2S$  ionization threshold. The energy shift is about 0.08 eV, which

for this particular resonant state  $3s3p$  translates into an error of 0.02 in the quantum defect. The interference pattern observed here is somewhat similar to the perturbation near the  $2p^4(^3P)3p(^2P)5s$  peak at 51.93 eV, in that the  $2p^4(^3P)3p(^2P)nl$  Rydberg series to the right of the  $3s3p$  perturber are strongly suppressed. As opposed to other resonances analyzed in this subsection, the  $n \geq 7$  members of the  $2p^4(^3P)3p(^2P)nl$  series exhibit weak, but observable, relativistic features, deriving from the target state fine-structure splitting of 15.8 meV. In the calculated spectrum, the fine-structure is manifested in the appearance of three intense series and two weaker series; in pure  $LS$  coupling, we expect only two  $2p^4(^3P)3p(^2P)nl\ ^1P^o$  series ( $l=s, d$ ). Eigenvector analysis showed that these resonances are characterized best in  $jK$  coupling. (Note, however, that  $jK$  and  $jj$  couplings are equally valid in the experimental spectrum, because the only observable quantum numbers are the spin-angular momentum  $j_c$  of the target, the angular  $l$  and principal quantum number  $n$  of a Rydberg electron. Intermediate quantum numbers, as  $j_o$  or  $K$ , can be deduced in other types of experiments, probing, for example, wave-function

TABLE VI. Parameters of the  $2p^4(^3P)3p(^2P)ns\ ^1P^o$  autoionizing Rydberg series. The  $n=3$  member of this series is equivalent to the  $2p^4(^3P)3s(^2P)3p\ ^1P^o$  resonance, which is already classified in Table IV. The  $n > 7$  members are classified according to  $jK$  coupling as  $[j_c, nl]K$ . Only the prominent members observed in the neon spectrum ( $K = \frac{3}{2}$ ) are listed.

$n$	$E_{\text{th}}$	$E_{\text{exp}}$	$E_{\text{Ref.}[2]}$	$\nu_{\text{th}}$	$\nu_{\text{exp}}$	$\nu_{\text{Ref.}[2]}$	$\Gamma_{\text{th}}$	$\Gamma_{\text{red}}$
4	51.18338	50.760(5)	50.749(7)	2.676	2.423(3)	2.417	0.137[-01]	0.264
5	52.03672	51.926(4)	51.928(7)	3.606	3.438(6)	3.441	0.272[-02]	0.128
6	52.43035	52.388(4)	52.387(7)	4.567	4.444(13)	4.44	0.816[-02]	0.777
7	52.64003	52.618(4)		5.544	5.446(24)		0.460[-02]	0.784
$[\frac{3}{2}, 8s]_{\frac{3}{2}}$	52.76229	52.7493(15)	52.737(20)	6.580	6.443(15)	6.32	0.316[-02]	0.899
$[\frac{3}{2}, 9s]_{\frac{3}{2}}$	52.83964	52.8320(15)	52.827(20)	7.578	7.452(23)	7.37	0.214[-02]	0.932
$[\frac{3}{2}, 10s]_{\frac{3}{2}}$	52.89159	52.8863(15)		8.576	8.447(33)		0.152[-02]	0.961
$[\frac{3}{2}, 11s]_{\frac{3}{2}}$	52.92820	52.9243(15)		9.576	9.44(5)		0.111[-02]	0.977
$[\frac{3}{2}, 12s]_{\frac{3}{2}}$	59.95489	52.9513(20)		10.574	10.40(8)		0.867[-03]	1.025

TABLE VII. Parameters of the  $2p^4(^3P)3p(^2P)nd^1P^o$  autoionizing Rydberg series. The  $n > 6$  members are classified according to the relativistic  $jK$  coupling as  $[j_c, nl]K$ . Only the prominent members observed in the neon spectrum ( $K = \frac{3}{2}$ ) are listed.

$n$	$E_{\text{th}}$	$E_{\text{exp}}$	$E_{\text{Ref.}[2]}$	$\nu_{\text{th}}$	$\nu_{\text{exp}}$	$\nu_{\text{Ref.}[2]}$	$\Gamma_{\text{th}}$	$\Gamma_{\text{red}}$
3	51.50422	51.308(4)	51.309(7)	2.936	2.773(3)	2.773	0.250[-01]	0.632
4	52.15869	52.110(4)	52.112(7)	3.837	3.751(8)	3.753	0.369[-02]	0.209
5	52.49938	52.474(4)	52.478(7)	4.829	4.750(16)	4.76	0.253[-02]	0.285
6	52.68293	52.660(15)	52.658(20)	5.834	5.71(10)	5.70	0.241[-02]	0.478
$[\frac{3}{2}, 7d] \frac{3}{2}$	52.78847	52.7767(15)		6.872	6.731(17)		0.110[-02]	0.355
$[\frac{1}{2}, 7d] \frac{3}{2}$	52.80432	52.7917(20)		6.873	6.722(22)		0.163[-02]	0.528
$[\frac{3}{2}, 8d] \frac{3}{2}$	52.85701	52.8493(15)		7.872	7.730(25)		0.593[-03]	0.289 <sup>a</sup>
$[\frac{1}{2}, 8d] \frac{3}{2}$	52.87262	52.8653(15)		7.869	7.733(25)		0.986[-03]	0.480
$[\frac{3}{2}, 9d] \frac{3}{2}$	52.90363	52.8977(15)		8.870	8.71(4)		0.478[-03]	0.334
$[\frac{1}{2}, 9d] \frac{3}{2}$	52.91924	52.9137(15)		8.865	8.72(4)		0.688[-03]	0.479
$[\frac{3}{2}, 10d] \frac{3}{2}$	52.93688	52.9333(15)		9.869	9.73(5)		0.346[-03]	0.333
$[\frac{1}{2}, 10d] \frac{3}{2}$	52.95250	52.9513(20)		9.863	9.81(7)		0.481[-03]	0.461
$[\frac{3}{2}, 11d] \frac{3}{2}$	52.96136	52.9587(15)		10.867	10.72(7)		0.308[-03]	0.396

<sup>a</sup> $\Gamma$  and  $\Gamma_{\text{red}}$  are not very accurate due to strongly overlapping features with nearby resonances.

purity in radiative lifetime measurements.) Their eigenvector compositions show that the three most intense series, indicated in Fig. 11(b) by the letters *a*, *b*, and *c*, have a common spin-angular momentum  $K = \frac{3}{2}$ . These levels are classified, in increasing order of energy, as:  $[^2P_{3/2}, ns] \frac{3}{2}$ ,  $[^2P_{3/2}, nd] \frac{3}{2}$ , and  $[^2P_{1/2}, nd] \frac{3}{2}$ , respectively. The experimental spectrum favors much more the  $[^2P_{3/2}, ns] \frac{3}{2}$ ,  $[^2P_{3/2}, nd] \frac{3}{2}$  peaks (*a* and *b*), whereas the third peak  $[^2P_{1/2}, nd] \frac{3}{2}$  (*c*) is more suppressed than in the calculations. The other two higher-lying members (not marked on Fig. 11) couple to a common spin-angular momentum  $K = \frac{1}{2}$ .

## VI. SUMMARY

Photoionization measurements of gaseous neon are reported in the photon-energy range between 44 and 53 eV. Numerous  $^1P^o$  resonances belonging to the singly excited Rydberg series  $2s2p^6np$  and the doubly excited Rydberg series  $2s^22p^43snp$  and  $2s^22p^43pnl$  ( $l = s, d$ ) have been observed in our 3-meV spectral resolution experiments. The singly excited Rydberg series  $2s2p^6np$  are resolved up to  $n > 20$ . This series overlaps with  $3s4p$  and  $3s5p$  members of the first doubly excited Rydberg series  $2p^4(^3P)3s(^2P)np$ , which splits—in the  $jj$  coupling ( $j_c, j_o$ )<sub>*n*</sub>—into two intense series  $(\frac{3}{2}, \frac{3}{2})_n$  and  $(\frac{1}{2}, \frac{1}{2})_n$ , and into two weaker series  $(\frac{3}{2}, \frac{1}{2})_n$  and  $(\frac{1}{2}, \frac{3}{2})_n$ . The higher members of the first three series, interacting with the  $2p^4(^1D)3s(^2D)3p$  perturber, are resolved up to  $n = 18$ , 18, and 8, respectively; the last series,  $(\frac{1}{2}, \frac{3}{2})_n$ , has not been observed. The upper photon energy range,  $h\nu > 50$  eV, is characterized by overlapping doubly excited  $2p^4(^1D)3s(^2D)np$  and  $2p^4(^3P)3p(^2P)nl$  ( $l = s, d$ ) Rydberg series, interacting

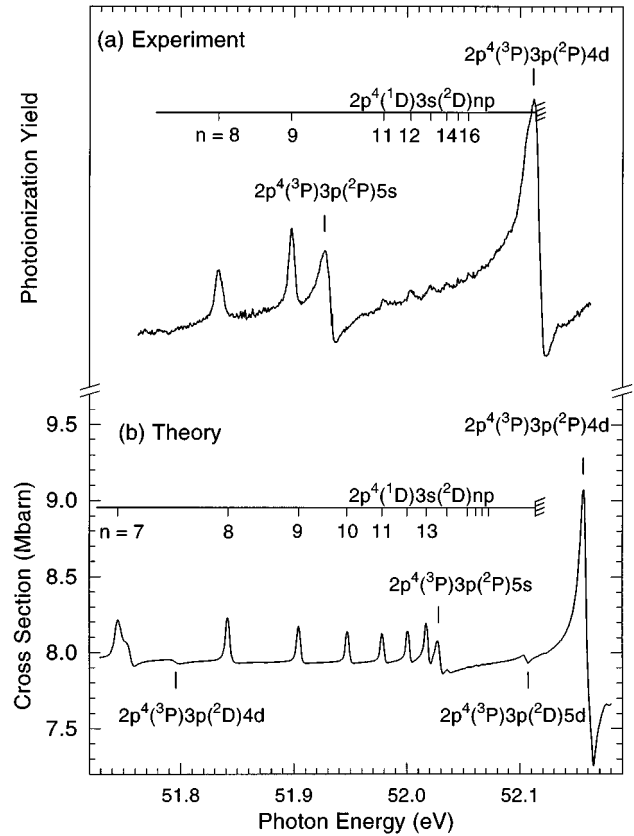


FIG. 10. Excited  $2p^4(^1D)3s(^2D)np^1P^o$  resonances perturbed by  $2p^4(^3P)3p(^2P)5s^1P^o$  and by  $2p^4(^3P)3p(^2P)4d^1P^o$ . The calculated cross section (b) also exhibits weak perturbations arising from  $n = 4$  and  $n = 5$  members of the  $2p^4(^3P)3p(^2D)nd$  Rydberg series which have not been observed in the experimental spectrum (a).

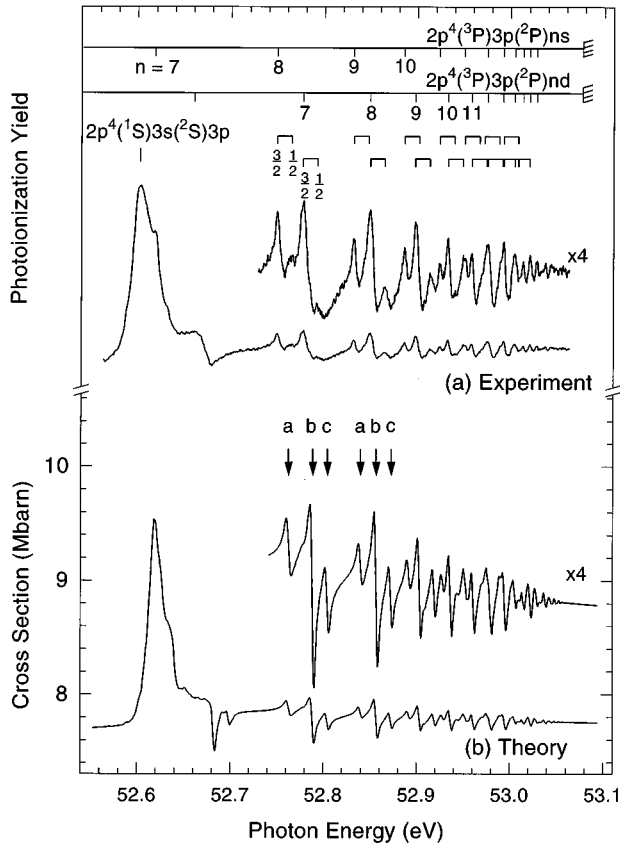


FIG. 11. Photoionization spectrum of  $2p^4(^3P)3p(^2P_{j_c})nl$  resonances ( $j_c = \frac{3}{2}, \frac{1}{2}; l = s, d$ ), plotted as a function of photon energy at and above the  $2p^4(^1S)3s(^2S)3p^1P^o$  perturber. In the experimental spectrum (a), the  $ns$  and  $nd$  series exhibit a relativistic splitting due to  $j_c$ : The experimental positions of the main resonances ( $j_c = \frac{3}{2}$ ) are marked in the upper two bar diagrams, while the positions of the weaker  $j_c = \frac{1}{2}$  resonances are given with a fixed distance between  $j_c = \frac{3}{2}$  and  $j_c = \frac{1}{2}$ , according to the threshold splitting of 15.8 meV. In the theoretical spectrum (b), the most intense Rydberg series members, labeled *a*, *b*, and *c*, are characterized in  $jK$  coupling as  $[^2P_{3/2}, ns]_{\frac{3}{2}}^{\frac{3}{2}}$ ,  $[^2P_{3/2}, nd]_{\frac{3}{2}}^{\frac{3}{2}}$ , and  $[^2P_{1/2}, nd]_{\frac{3}{2}}^{\frac{3}{2}}$ , respectively. The resonances *a*, *b* and *c* corresponds to  $2p^4(^3P)3p(^2P_{3/2})ns$ ,  $2p^4(^3P)3p(^2P_{3/2})nd$  and  $2p^4(^3P)3p(^2P_{1/2})nd$ , respectively.

together and with a few other perturbers. The  $2p^4(^3P)3p(^2P)nl$  ( $l = s, d$ ) series again splits due to relativistic effects. Most of these experimental features are very clearly resolved, which stimulated us to perform detailed calculations in this energy range.

The theoretical studies included the eigenchannel  $R$ -matrix method, multichannel quantum-defect theory, and the recoupling-frame transformation. These nearly *ab initio* methods account for most of the observed features, including a class of relativistic effects. On an average, the calculated quantum defects differ from the experimental values by about 0.02–0.04, and resonance widths and profiles are also in reasonable agreement with the experiment. For the majority of the observed resonances, this accuracy is sufficient for the unambiguous classification of the resonances. In addition to a standard line-by-line comparison with the experiment, we conducted detailed studies of various perturbations in the spectra. In particular, we explained the enhancement of the lowest  $2p^4(^3P)3s(^2P)3p^1P^o$  resonance, and the near-vanishing of the  $3s4p$  and  $3s5p$  members of this Rydberg series. Furthermore, we investigated variations in intensities and quantum defects of the fine-structure split  $2p^4(^3P)3s(^2P_{j_c})npj_o$  resonances, adopting the methodology of Lu-Fano plots for autoionizing Rydberg states. We also explained variations in autoionization widths of  $2p^4(^1D)3s(^2D)np^1P^o$  Rydberg series, where the first  $3p$  member appear to be much narrower than the  $4p$  member, counterintuitive to the scaling rule  $\Gamma \sim \nu^{-3}$ .

## ACKNOWLEDGMENTS

The authors acknowledge valuable discussions with D. A. Shirley and T. Gorczyca in the initial stages of this work. This work was supported by the Bundesminister für Bildung, Wissenschaft, Forschung und Technologie, Project No. 05-650-KEA, the Deutsche Forschungsgemeinschaft, Project No. Do 561/1-1 and the Division of Chemical Sciences, Office of Basic Energy Sciences, Office of Energy Research, U.S. Department of Energy, Grant No. DE-FG03-94ER14413.

- [1] A. A. Wills, A. A. Cafola, A. Svensson, and J. Comer, *J. Phys. B* **23**, 2013 (1990).
- [2] K. Codling, R. P. Madden, and D. L. Ederer, *Phys. Rev.* **155**, 26 (1967).
- [3] M. Domke, T. Mandel, A. Puschmann, X. Xue, D. A. Shirley, G. Kaindl, H. Petersen, and P. Kuske, *Rev. Sci. Instrum.* **63**, 80 (1992).
- [4] M. Domke, G. Remmers, and G. Kaindl, *Nucl. Instrum. Methods Phys. Res. Sect. B* **87**, 173 (1994).
- [5] M. Domke, C. Xue, A. Puschmann, T. Mandel, E. Hudson, D. A. Shirley, G. Kaindl, C. H. Greene, and H. R. Sadeghpour, *Phys. Rev. Lett.* **66**, 1306 (1991).
- [6] M. Domke, G. Remmers, and G. Kaindl, *Phys. Rev. Lett.* **69**, 1171 (1992).
- [7] M. Domke, K. Schulz, G. Remmers, G. Kaindl, and D. Wintgen, *Phys. Rev. A* **53**, 1424 (1996).
- [8] W. F. Chan, G. Cooper, X. Guo, and C. E. Brion, *Phys. Rev. A* **45**, 1420 (1992).
- [9] G. Kaindl, K. Schulz, P. A. Heimann, J. D. Bozek, and A. S. Schlachter, *Synchr. Rad. News* **8**(5), 29 (1995).
- [10] V. Schmidt, *Rep. Prog. Phys.* **55**, 1483 (1992).
- [11] W. R. Johnson, K. T. Cheng, K.-N. Huang, and M. Le Dour-

- neuf, Phys. Rev. A **22**, 989 (1980); W. R. Johnson and M. Le Dourneuf, J. Phys. B **13**, L13 (1980).
- [12] P. G. Burke and K. T. Taylor, J. Phys. B **8**, 2620 (1975).
- [13] A. Hibbert and M. P. Scott, J. Phys. B **27**, 1315 (1994).
- [14] M. Stener, P. Decleva, and A. Lisini, J. Phys. B **28**, 4973 (1995).
- [15] F. A. Parpia, W. R. Johnson, and V. Radojević, Phys. Rev. A **29**, 3173 (1984).
- [16] W. Wijesundera and H. P. Kelly, Phys. Rev. A **39**, 634 (1989).
- [17] C. H. Greene, Phys. Rev. A **32**, 1880 (1985); C. H. Greene, in *Fundamental Processes of Atomic Dynamics*, edited by J. S. Briggs, H. Kleinpoppen, and H. O. Lutz (Plenum, New York, 1988), p. 105.
- [18] F. Robicheaux and C. H. Greene, Phys. Rev. A **46**, 3821 (1992); **47**, 1066 (1993).
- [19] F. Robicheaux and C. H. Greene, Phys. Rev. A **48**, 4429 (1993).
- [20] G. Miecnik and C. H. Greene, J. Opt. Soc. Am. B **13**, 1 (1996).
- [21] H. Petersen, Opt. Commun. **40**, 402 (1982).
- [22] W. Persson, Phys. Scr. **3**, 133 (1971).
- [23] S. Bashkin and J. O. Stoner, *Atomic Energy Levels and Grotian Diagrams* (North Holland, Amsterdam, 1975), p. 291.
- [24] E. R. Cohen and B. N. Taylor, Rev. Mod. Phys. **59**, 1121 (1987).
- [25] M. J. Seaton, Rep. Prog. Phys. **46**, 167 (1983).
- [26] U. Fano, Phys. Rev. A **2**, 353 (1970); C. M. Lee and K. T. Lu, *ibid.* **8**, 1241 (1973); C. H. Greene and M. Aymar, *ibid.* **44**, 1773 (1991).
- [27] C. Froese Fischer, *The Hartree-Fock Method for Atoms* (Wiley & Sons, New York, 1977).
- [28] L. I. Schiff, *Quantum Mechanics* (McGraw-Hill, New York, 1968).
- [29] M. Aymar and C. H. Greene, Rev. Mod. Phys. (to be published).
- [30] C. Froese Fischer, Comput. Phys. Commun. **64**, 369 (1991).
- [31] H. Smid and J. E. Hansen, J. Phys. B **14**, L811 (1981).
- [32] F. Robicheaux (private communication).
- [33] R. D. Cowan, *The Theory of Atomic Structure and Spectra* (University of California Press, Berkeley, 1981).
- [34] H. A. Bethe and E. E. Salpeter, *Quantum Mechanics of One- and Two-Electron Atoms* (Plenum, New York 1977).
- [35] F. Robicheaux, Phys. Rev. A **48**, 4162 (1993).
- [36] M. Domke, K. Schulz, G. Remmers, A. Gutiérrez, G. Kaindl, and D. Wintgen, Phys. Rev. A **51**, R4309 (1995).
- [37] R. L. Kelly, J. Phys. Chem. Data **16**, Suppl. 1 (1987); see also I. I. Sobel'man, *Introduction to the Theory of Atomic Spectra* (Pergamon Press, Oxford, 1972), p. 53.
- [38] K. T. Lu and U. Fano, Phys. Rev. A **2**, 81 (1970); see also T. F. Gallagher, *Rydberg Atoms* (Cambridge University Press, Cambridge, 1994), p. 453, and references therein.
- [39] C. H. Greene and M. Aymar (unpublished).
- [40] G. Miecnik, R. Robicheaux, and C. H. Greene, Phys. Rev. A **51**, 513 (1995).